The Astrophysical Journal Supplement Series, 261:5 (29pp), 2022 July https://doi.org/10.3847/1538-4365/ac6602

BASS. XXV. DR2 Broad-line-based Black Hole Mass Estimates and Biases from Obscuration

Julian E. Mejía-Restrepo[1], Benny Trakhtenbrot[2], Michael J. Koss[3,4], Kyuseok Oh[5,6,32], Jakob den Brok[7], Daniel Stern[8], Meredith C. Powell[9], Federica Ricci[10,11,12], Turgay Caglar[13], Claudio Ricci[14,15], Franz E. Bauer[4,12,16,17], Ezequiel Treister[12], Fiona A. Harrison[18], C. M. Urry[19], Tonima Tasnim Ananna[20], Daniel Asmus[21], Roberto J. Assef[22], Rudolf E. Bär[23], Patricia S. Bessiere[12,24], Leonard Burtscher[13], Kohei Ichikawa[25], Darshan Kakkad[1,26], Nikita Kamraj[18], Richard Mushotzky[27], George C. Privon[28,29], Alejandra F. Rojas[30], Eleonora Sani[1], Kevin Schawinski[31], and Sylvain Veilleux[27]

[1] European Southern Observatory, Casilla 19001, Santiago 19, Chile; julianmejia@gmail.com
[2] School of Physics and Astronomy, Tel Aviv University, Tel Aviv 69978, Israel
[3] Eureka Scientific, 2452 Delmer Street, Suite 100, Oakland, CA 94602-3017, USA
[4] Space Science Institute, 4750 Walnut Street, Suite 205, Boulder, CO 80301, USA
[5] Korea Astronomy & Space Science institute, 776, Daedeokdae-ro, Yuseong-gu, Daejeon 34055, Republic of Korea
[6] Department of Astronomy, Kyoto University, Kitashirakawa-Oiwake-cho, Sakyo-ku, Kyoto 606-8502, Japan
[7] Argelander-Institut fur Astronomie, Universität Bonn, Auf dem Hügel 71, D-53121 Bonn, Germany
[8] Jet Propulsion Laboratory, California Institute of Technology, 4800 Oak Grove Drive, MS 169-224, Pasadena, CA 91109, USA
[9] Kavli Institute of Particle Astrophysics and Cosmology, Stanford University, 452 Lomita Mall, Stanford, CA 94305, USA
[10] Dipartimento di Fisica e Astronomia, Universitá di Bologna, via Piero Gobetti 93/2, I-40129 Bologna, Italy
[11] INAF—Osservatorio di Astrofisica e Scienza dello Spazio di Bologna, Via Gobetti, 93/3, I-40129 Bologna, Italy
[12] Instituto de Astrofísica, Facultad de Física, Pontificia Universidad Católica de Chile, Casilla 306, Santiago 22, Chile
[13] Leiden Observatory, PO Box 9513, 2300 RA, Leiden, The Netherlands
[14] Núcleo de Astronomía de la Facultad de Ingeniería, Universidad Diego Portales, Av. Ejército Libertador 441, Santiago, Chile
[15] Kavli Institute for Astronomy and Astrophysics, Peking University, Beijing 100871, People's Republic of China
[16] Centro de Astroingeniería, Pontificia Universidad Católica de Chile, Av. Vicuña Mackenna 4860, 7820436 Macul, Santiago, Chile
[17] Millennium Institute of Astrophysics (MAS), Nuncio Monseñor Sótero Sanz 100, Providencia, Santiago, Chile
[18] Cahill Center for Astronomy and Astrophysics, California Institute of Technology, Pasadena, CA 91125, USA
[19] Yale Center for Astronomy & Astrophysics, Physics Department, Yale University, PO Box 201820, New Haven, CT 06520-8120, USA
[20] Department of Physics & Astronomy, Dartmouth College, 6127 Wilder Laboratory, Hanover, NH 03755, USA
[21] Department of Physics & Astronomy, University of Southampton, Southampton, Hampshire, SO17 1BJ, UK
[22] Núcleo de Astronomía de la Facultad de Ingeniería y Ciencias, Universidad Diego Portales, Av. Ejército Libertador 441, Santiago 8370191, Chile
[23] Institute for Particle Physics and Astrophysics, ETH Zürich, Wolfgang-Pauli-Strasse 27, CH-8093 Zürich, Switzerland
[24] Instituto de Astrofísica de Canarias (IAC), C/Vía Láctea, s/n, E-38205, La Laguna, Tenerife, Spain
[25] Frontier Research Institute for Interdisciplinary Sciences, Tohoku University, Sendai 980-8578, Japan
[26] Department of Physics, University of Oxford, Denys Wilkinson Building, Keble Road, Oxford, OX1 3RH, UK
[27] Department of Astronomy and Joint Space-Science Institute, University of Maryland, College Park, MD 20742, USA
[28] National Radio Astronomy Observatory, 520 Edgemont Road, Charlottesville, VA 22903, USA
[29] Department of Astronomy, University of Florida, 211 Bryant Space Sciences Center, Gainesville, FL 32611, USA
[30] Centro de Astronomia (CITEVA), Universidad de Antofagasta, Avenida Angamos 601, Antofagasta, Chile
[31] Modulos AG, Technoparkstrasse 1, CH-8005 Zurich, Switzerland
Received 2021 March 31; revised 2022 March 11; accepted 2022 March 14; published 2022 July 15

Abstract

We present measurements of broad emission lines and virial estimates of supermassive black hole masses ($M_{\rm BH}$) for a large sample of ultrahard X-ray-selected active galactic nuclei (AGNs) as part of the second data release of the BAT AGN Spectroscopic Survey (BASS/DR2). Our catalog includes $M_{\rm BH}$ estimates for a total of 689 AGNs, determined from the Hα, Hβ, Mg II λ2798, and/or C IV λ1549 broad emission lines. The core sample includes a total of 512 AGNs drawn from the 70 month Swift/BAT all-sky catalog. We also provide measurements for 177 additional AGNs that are drawn from deeper Swift/BAT survey data. We study the links between $M_{\rm BH}$ estimates and line-of-sight obscuration measured from X-ray spectral analysis. We find that broad Hα emission lines in obscured AGNs ($\log(N_{\rm H}/{\rm cm}^{-2}) > 22.0$) are on average a factor of $8.0^{+4.1}_{-2.4}$ weaker relative to ultrahard X-ray emission and about 35^{+7}_{-12}% narrower than those in unobscured sources (i.e., $\log(N_{\rm H}/{\rm cm}^{-2}) < 21.5$). This indicates that the innermost part of the broad-line region is preferentially absorbed. Consequently, current single-epoch $M_{\rm BH}$ prescriptions result in severely underestimated (>1 dex) masses for Type 1.9 sources (AGNs with broad Hα but no broad Hβ) and/or sources with $\log(N_{\rm H}/{\rm cm}^{-2}) \gtrsim 22.0$. We provide simple multiplicative corrections for the observed luminosity and width of the broad Hα component (L[bHα] and FWHM[bHα]) in such sources to account for this effect and to (partially) remedy $M_{\rm BH}$ estimates for Type 1.9 objects. As a key ingredient of BASS/DR2,

[32] JSPS Fellow.

our work provides the community with the data needed to further study powerful AGNs in the low-redshift universe.

Unified Astronomy Thesaurus concepts: Active galactic nuclei (16); Surveys (1671); Catalogs (205); Supermassive black holes (1663); X-ray surveys (1824); M-sigma relation (2026); Seyfert galaxies (1447)

Supporting material: machine-readable tables

1. Introduction

Accurate estimates of supermassive black hole (SMBH) masses ($M_{\rm BH}$) in active galactic nuclei (AGNs) are critical to understanding SMBH demographics and growth and their apparent coevolution with their host galaxies (e.g., Ferrarese & Merritt 2000; Kormendy & Ho 2013). This requires large, highly complete surveys of AGNs (and SMBHs in general), as well as a detailed characterization of the different sources of uncertainties involved in the currently available methods to estimate $M_{\rm BH}$.

In unobscured AGNs, $M_{\rm BH}$ is commonly determined through the so-called "single epoch" (SE), or "virial" BH mass estimation method, which uses detailed spectral measurements probing the broad-emission-line region (BLR; see, e.g., works by Greene & Ho 2005; Wang et al. 2009; Shen & Liu 2012; Trakhtenbrot & Netzer 2012; Mejía-Restrepo et al. 2016; or reviews by Shen 2013; Peterson 2014). This method is based on (1) the assumption of virialized motion of the BLR gas and (2) empirical relations between the (accretion-related) continuum luminosity and the BLR size. These latter relations are calibrated in reverberation mapping (RM) experiments and take the general form $R_{\rm BLR} \propto L_\lambda^\alpha$, where L_λ is the monochromatic luminosity at a particular wavelength λ (e.g., Kaspi et al. 2000, 2005; Bentz et al. 2009; Park et al. 2012; Bentz et al. 2013). Under these assumptions, the width of the broad-emission-line profiles, such as the FWHM, can be used as a proxy for the virial velocity of the BLR clouds, $v_{\rm BLR}$. $M_{\rm BH}$ can thus be expressed as

$$M_{\rm BH} = G^{-1} R_{\rm BLR}\, v_{\rm BLR}^2 \propto f\, L_\lambda^\alpha\, {\rm FWHM}^2. \quad (1)$$

Here, G is the gravitational constant and f is a geometrical factor that accounts for the unknown structure and inclination of the BLR with respect to the line of sight. The $R_{\rm BLR}({\rm H}\beta) - L_\lambda(5100\,\text{Å})$ relation is the only $R_{\rm BLR}-L_\lambda$ relation that has been established for a large number of AGNs covering a broad luminosity range, $10^{43} \lesssim L_{5100}/{\rm erg\,s^{-1}} \lesssim 10^{47}$ (Bentz et al. 2013; Bentz & Katz 2015). Consequently, it has been used to calibrate several other SE $M_{\rm BH}$ prescriptions, using other emission lines and/or continuum bands (e.g., McLure & Jarvis 2002; Greene & Ho 2005; Trakhtenbrot & Netzer 2012).

Single-epoch mass prescriptions have allowed the estimation of $M_{\rm BH}$ for tens of thousands of AGNs in large spectroscopic surveys (e.g., Shen et al. 2008; Kozłowski 2017) and have thus allowed the probing of the evolution of the active SMBH population (e.g., Greene & Ho 2007; Vestergaard & Osmer 2009; Schulze & Wisotzki 2010; Trakhtenbrot & Netzer 2012; Kelly & Shen 2013; Schulze et al. 2015) and of the links between SMBHs and their hosts (e.g., Jahnke et al. 2009; Decarli et al. 2010; Merloni et al. 2010; Bongiorno et al. 2014; Suh et al. 2020) out to the highest accessible redshifts (e.g., Mazzucchelli et al. 2017; Shen et al. 2019). Most of these studies, and particularly those dedicated to the largest samples and/or the highest-redshift ones (i.e., $z > 3$), had to be based on surveys of luminous, unobscured, and optically selected AGNs (e.g., SDSS quasars).

Despite these significant achievements, the SE approach should be used with care as it is subject to several significant (systematic) uncertainties that, in principle, may total 0.4 dex in $M_{\rm BH}$, or even more (e.g., Shen 2013; Pancoast et al. 2014a; Peterson 2014). Below, we briefly describe the most critical uncertainties relevant to the current work. A major source of uncertainty stems from the need to assume a structural geometrical factor, f. The common approach is to deduce a universal f by requiring that RM-based BH masses match those expected from the relation between $M_{\rm BH}$ and the stellar velocity dispersion (σ_*) found in local galaxies (Onken et al. 2004; Graham 2016; Woo et al. 2015; Batiste et al. 2017). Some studies, however, have put forward the idea that the BLR may have a disk-like structure, at least in some AGNs (e.g., Eracleous & Halpern 1994; Grier et al. 2013; Pancoast et al. 2014b; Mejía-Restrepo et al. 2018a, and references therein). Such a distribution of gas would introduce a bias to the SE $M_{\rm BH}$ determination, as the (unknown) inclination angle of the BLR disk with respect to the line of sight, for each AGN, limits the ability to measure the true virial velocity. In particular, BH masses would be overestimated (underestimated) at larger (smaller) inclination angles (e.g., Collin et al. 2006; Shen & Ho 2014; Mejía-Restrepo et al. 2018a).

Another important bias comes from the possible presence of winds, which could potentially affect the (observed) BLR gas dynamics. Indeed, several studies have shown that high-ionization lines such as C IV λ1549, commonly used to estimate $M_{\rm BH}$ at $z \gtrsim 2$, show highly blueshifted profiles (by up to 8000 km s^{-1}; e.g., Marziani et al. 2015; Vietri et al. 2020, and references therein), and thus their line widths are known to be poorer tracers of the virial velocity of the BLR gas, compared to other lines (e.g., Richards et al. 2011; Coatman et al. 2016; Mejía-Restrepo et al. 2018b). In the case of the Mg II λ2798 line, several studies have shown that the innermost, highest-velocity gas is affected by fountain-like winds, and the global virial assumption is likely no longer valid for systems with FWHM $\gtrsim 6000\,{\rm km\,s^{-1}}$ (e.g., Trakhtenbrot & Netzer 2012; Marziani et al. 2013; Popović et al. 2019).

Unlike the aforementioned biases, the partial obscuration of the broad-line-emitting region and its potential effect on $M_{\rm BH}$ estimates remains poorly understood. Gaskell & Harrington (2018) proposed that compact outflowing dusty clumps, driven by radiation pressure, may partially block the BLR emission. Such partial obscuration may explain the lack of correlation between disk and BLR line variabilities occasionally reported in RM campaigns (e.g., Goad et al. 1999; Cackett et al. 2015; Goad et al. 2016). Preliminary observational evidence for this comes from the recent study of Caglar et al. (2020), who identified a systematic offset of roughly −0.6 dex between the broad-Hα-based $M_{\rm BH}$ estimates and those based on the stellar velocity dispersion in 19 hard X-ray-selected AGNs drawn from the volume-complete LLAMA sample (Davies et al. 2015), including both unobscured and partially obscured

systems (as deduced from the relative strength of the broad Hβ line). Further support for the idea that this discrepancy could be (partially) attributed to dust obscuration comes from the fact that the discrepancy is found to be more dramatic in systems that completely lack broad Hβ emission (Type 1.9 AGNs; see also Goodrich 1989, 1990; Ricci et al. 2017c).

One way to overcome these complications is to focus on the (rest-frame) near-infrared (NIR) regime, which is at least 10 times less sensitive to extinction than the optical. Ricci et al. (2017d) have provided SE $M_{\rm BH}$ prescriptions that rely on several broad NIR lines (Paα, Paβ, and He I λ1.083 μm) and on the hard X-ray continuum luminosity (in either the 2–10 keV and/or the 14–195 keV regime) as BLR probes. In addition to the advantages in overcoming obscuration, the use of the hard X-ray luminosity allows the measurement of $M_{\rm BH}$ even in low-luminosity systems, where host contamination significantly affects optical AGN continuum estimates. One further advantage of this approach is that it can be applied even to some Type 2 AGNs—the so-called hidden BLR Type 2s, where broad lines are detected in the NIR regime while the optical spectrum shows only narrow Hβ and/or Hα (see e.g., Veilleux et al. 1997a, 1997b, 1999; Riffel et al. 2006; Lamperti et al. 2017; Onori et al. 2017; den Brok et al. 2022). However, calibrating the relevant prescription(s) requires larger data sets of high signal-to-noise NIR spectra in order to improve the reliability of the method and better characterize the obscuration effects in Type 2 AGNs.

In order to further investigate all these issues, one has to obtain high-quality optical-NIR spectroscopy of broad AGN emission lines and robust, independent line-of-sight obscuration measures for a large AGN sample that is unbiased with regard to obscuration. The BAT AGN Spectroscopic Survey (BASS) has been collecting and analyzing optical and NIR spectroscopy, X-ray spectral observations, and other multi-wavelength data for bright AGNs selected in the ultrahard X-rays (14–195 keV) by the Swift/BAT mission. The first data release of BASS (DR1; Koss et al. 2017; Lamperti et al. 2017; Ricci et al. 2017a) has already provided $M_{\rm BH}$ estimates for hundreds of AGNs, over a wide range of obscuration, drawn from the 70 month catalog of Swift/BAT (Baumgartner et al. 2013). This highly complete and rich collection of multi-wavelength data has already been used in several studies that examined the links between AGN physics, structure, and various emission components, specifically to investigate topics where obscuration and/or orientation may play a key role (e.g., Ricci et al. 2017b; Shimizu et al. 2018; Bär et al. 2019; Rojas et al. 2020).

In this paper we present broad-emission-line measurements as part of the second data release of the BAT AGN Spectroscopic Survey (BASS/DR2), including the analysis of hundreds of new spectra and improved estimates of the BH masses of hundreds of AGNs, thus greatly improving and expanding on the first data release described in Koss et al. (2017). We then combine these new measurements with the rich BASS/DR2 multiwavelength data set to explore the effect of dust obscuration on single-epoch $M_{\rm BH}$ estimates from optical broad emission lines. Other BASS/DR2 studies present extensive NIR spectroscopy and use it to address complementary issues (den Brok et al. 2022; Ricci et al. 2022). Throughout this work, we adopt $\Omega_{\rm M}=0.3$, $\Omega_{\Lambda}=0.7$, and $H_0=70\,{\rm km\,s^{-1}\,Mpc^{-1}}$.

2. Data Content and Analysis

2.1. Overview of Survey, Sample, and Data Content

The ultimate goal of BASS is to complement the largest available sample of Swift/BAT, hard X-ray-selected AGNs with optical spectroscopy and ancillary multiwavelength data using dedicated observations and archival data and thus to complete the first large survey ($\gtrsim$1000 sources) of the most powerful accreting SMBHs in the low-redshift universe. This work is part of a series of papers devoted to the 2nd Data Release (DR2) of BASS. In particular, this paper presents detailed spectral measurements of broad-line AGNs, with either a broad Hβ or Hα lines (i.e., FWHM $>1000\,{\rm km\,s^{-1}}$), as well as a smaller subset of higher-redshift sources with Mg II and C IV broad emission lines. Koss et al. (2022a) provide an overview of BASS DR2, while Koss et al. (2022b) provide a detailed account of the BASS/DR2 AGN catalog and main observational data, in particular the optical spectroscopy that is used here. Other key BASS DR2 papers include Koss et al. (2022c), where we present the velocity dispersion measurements for (obscured) BASS sources; Oh et al. (2022), where we focus on spectral measurements for narrow-line AGNs and host-light decomposition; and den Brok et al. (2022) and Ricci et al. (2022), where we present extensive NIR spectroscopic observations and analyze (broad) hydrogen and high-ionization (coronal) emission lines. The broad-line measurements and related $M_{\rm BH}$ (and $L/L_{\rm Edd}$) estimates presented herein are used in Ananna et al. (2022) to determine the BH mass and Eddington ratio distribution functions among essentially all BASS/DR2 AGNs.

BASS/DR1 used mostly archival telescope data (see, e.g., Figure 1 in Koss et al. 2017) for 641 BAT AGNs, including >250 spectra from the SDSS and 6dF surveys. In this DR2 paper, we provide a complete sample of BH mass estimates from optical broad emission lines for 512 AGNs with such lines in the 70 month Swift/BAT survey (Baumgartner et al. 2013). As part of our efforts toward DR2, we obtained new spectroscopy for many AGNs that did not have reliable BH mass determination in DR1. This includes (1) AGNs that did not have sufficient data (or data quality) to yield a BH mass measurement, including cases where the DR1 archival spectra were not properly flux calibrated (e.g., 6dF/2dF spectra; Jones et al. 2009); (2) Type 1.9 AGNs that were lacking a sufficiently high-quality spectrum to derive their BH masses, i.e., either a high-quality spectrum of their broad Hα lines or a spectrum that enables a robust velocity dispersion measurement; and (3) any DR1 AGN with only a broad-Hβ-line measurement, where Hα coverage was missing.

The new BASS/DR2 spectroscopic observations were carried out with a variety of facilities and instruments, as detailed in the main DR2 Catalog and Data paper (Koss et al. 2022b). Here we note that the large majority of new spectra were obtained with either the Double Beam Spectrograph (DBSP) mounted on the Hale 5 m telescope at Palomar observatory (Oke & Gunn 1982; >400 AGNs, mainly northern targets); the X-Shooter spectrograph at the Very Large Telescope (Vernet et al. 2011; >200 sources, mainly southern); or the Goodman spectrograph mounted on the SOAR telescope at Cerro Pachon (Clemens et al. 2004; >150 sources, also southern). More details on the facilities used, the spectroscopic setups and spectral resolutions, the observations, and the reduction procedures, can be found in Koss et al. (2022b).

The DR2 also includes publicly available optical spectroscopy from the SDSS (∼150 sources; drawn from SDSS DR16, Ahumada et al. 2020) and a small number of additional archival spectra, obtained as part of follow-up observations of ROSAT sources (Grupe et al. 1998, 1999). Finally, it includes spectra from recent studies of newly identified BAT AGNs (see Rojas et al. 2017).

In a nonnegligible number of cases, the extensive data-collecting process resulted in multiple optical spectra of the same source. In such cases, we select for each AGN the single best spectrum for broad-line-based $M_{\rm BH}$ measurements and use it in the present analysis (i.e., in Sections 3 and 4). This selection is done by considering the signal-to-noise ratio, spectral resolution, and quality of our spectral fits (see Section 2.3 below). Following this selection, our data set consists of a total of 559 unique AGNs with at least one useful optical spectrum. These 559 AGNs cover the redshift range $z\sim 0-4$, with the vast majority (>90%) being at $z\lesssim 0.5$.

All BASS DR2 spectra used here have sufficient spectral resolution to robustly measure the broad emission lines that are at the heart of the present paper. As noted, the main DR2 Catalog and Data paper (Koss et al. 2022b) provides ample details about the new, the previously obtained (DR1), and the archival spectra used throughout BASS DR2.

As mentioned above, the BASS/DR2 sample is fundamentally based on AGNs identified through the 70 month Swift/BAT catalog. However, the broad-line measurements described in the present study were also carried out on the optical spectra of 207 additional AGNs, which were acquired as part of ongoing BASS efforts to follow up on the increasingly deeper (and larger) content of the Swift/BAT all-sky survey (e.g., Oh et al. 2018). While we provide these measurements, we stress that this "bonus" sample is neither complete nor final: It does not represent any sort of flux- or volume-complete subset of deeper BAT data, and it is possible that future BASS follow-up observations and analyses could reveal significant changes to the determinations of optical counterparts, their redshifts, their AGN nature, and/or any other property. Apart from providing the relevant spectral measurements, we ignore this bonus sample throughout the rest of this paper. In particular, we do not include the bonus sample measurements when further discussing the BASS broad-line AGN statistics, measurements, or implications for any of the analyses we present (unless explicitly mentioned otherwise). A summary of the number of $M_{\rm BH}$ estimations from the Hα, Hβ, Mg II, and C IV broad emission lines is presented in Table 1.

The data reduction and analysis for the DR2 have maintained the same uniform approach described in the initial DR1 paper (Koss et al. 2017). All the spectra were processed using standard tasks (in IRAF or comparable reduction frameworks) for cosmic-ray removal, 1D spectral extraction, and wavelength and flux calibrations. The spectra were flux calibrated using standard stars, which were typically observed twice per night, whenever possible. In the DR2, we have also implemented the use of the `molecfit` software (Smette et al. 2015) to correct spectral regions affected by telluric absorption (e.g., H_2O, CO_2, CH_4, and O_2), based on nightly weather data (Koss et al. 2022a, 2022b).

2.2. Continuum and Line Emission Modeling

For each of the 559 broad-line-emitting sources in BASS with optical spectroscopy of either one of the Hα, Hβ, Mg II λ2798, and/or C IV λ1549 broad emission lines, we fitted the spectral complexes around these lines following the established and well-tested procedures initially presented in Trakhtenbrot & Netzer (2012) and further developed in Mejía-Restrepo et al. (2016), where more details can be found.

We note that the spectral modeling of narrow-line (i.e., Type 2) AGNs in BASS/DR2, and generally host-galaxy decomposition and narrow-line emission (including beyond the spectral regions considered here), was carried out independently, using a different fitting procedure, and is described in a dedicated BASS/DR2 paper (Oh et al. 2022). In Section 3 we show a few basic properties of the BASS/DR2 Type 2 AGN population, based on this independent spectral analysis, which is however not used in any other part of the present study.

The broad-line-fitting procedures use the `PySpecKit` Python package (Ginsburg & Mirocha 2011) to measure broad-emission-line properties. In brief, each spectrum is first corrected for Milky Way (foreground) dust extinction, using the Schlegel et al. (1998) maps and the Cardelli et al. (1989) extinction law (with $R_{\rm V}=3.1$). Next, the continuum emission is modeled with a (local) power law, fitted to certain continuum-dominated bands around the emission-line complex of interest (see Table 1 in Mejía-Restrepo et al. 2016). After subtracting the continuum emission, we proceed with the emission-line modeling as follows. Narrow-line components, including the [O III] $\lambda\lambda$4959,5007, [N II] $\lambda\lambda$6548,6584, and [S II] $\lambda\lambda$6717,6731 lines, as well as the narrow components of the Hα and Hβ lines, are modeled with a single Gaussian profile, each, except for rare cases where a visual inspection of the residuals motivated us to use an additional Gaussian. The widths and relative (velocity) shifts of these (primary) narrow profiles are tied to each other to avoid overfitting in heavily blended line complexes such as the Hα spectral complex. The profiles of the most prominent broad lines (Hα, Hβ, Mg II, and C IV) are modeled using two broad Gaussian components (each), while weaker emission lines are modeled with a single broad Gaussian (including He II λ1640, N IV λ1718, and Si III] λ1892). We emphasize that the two broad Gaussian components are used only in order to account for the total broad-emission-line profiles, and we do not consider any physical interpretation of the two separate components. This choice is based on previous works, which showed that two

Table 1
Summary of Good and Acceptable $M_{\rm BH}$ Estimations from Different Broad Emission Lines (See Section 2.3)

Subset	Hα	Hβ	Mg II	C IV	Total Objects[b]
70 m nonbeamed	434	343	3	0	445
70 m beamed	23	38	25	22	67
Total 70 m	457	381	28	22	512
Bonus 105m[a]	140	109	17	5	177
Total objects	597	490	45	27	689

Notes. Bonus 105 m objects correspond to additional sources drawn from deeper-than-70 month DR2 Swift/BAT survey data.
[a] Apart from providing the relevant spectral measurements, we ignore this bonus sample throughout the rest of this paper.
[b] Because there are objects with several $M_{\rm BH}$ estimations from different broad emission lines (e.g., Hα, Hβ, Mg II, and C IV), the total number of objects is smaller than the sum of available $M_{\rm BH}$ measurements from the different emission lines.

broad Gaussian components provide a good compromise between the number of free parameters (i.e., six) and the achieved goodness of fit (e.g., Shang et al. 2007; Trakhtenbrot & Netzer 2012; Mejía-Restrepo et al. 2016). All broad-emission features are restricted to have FWHM $> 1000\,\mathrm{km\,s^{-1}}$ and to be broader than the narrow emission features (including of the same transition; see above). We allow the central wavelength of each Gaussian component to be shifted by up to $1500\,\mathrm{km\,s^{-1}}$ relative to the laboratory central wavelength of the transition. The blueshift of the C IV and He II $\lambda1640$ components is allowed to be larger, up to $5000\,\mathrm{km\,s^{-1}}$, in agreement with what is observed in other large AGN samples (e.g., Shang et al. 2007; Runnoe et al. 2014; Coatman et al. 2017). We verified that yet larger shifts are neither observed in our sample nor required in our modeling of the spectra. When fitting the Hβ, Mg II, and C IV spectral complexes, we also account for (heavily blended) Fe II and Fe III transitions using the iron template described in Mejía-Restrepo et al. (2016), broadened and shifted separately for each source. Because the Mg II spectral complex was modeled using a relatively narrow, "local" part of the spectrum (ranging ∼2600–3000 Å in the rest frame), we did not include a designated model for the Balmer continuum. Instead, in our modeling approach, the Balmer continuum is assumed to be blended with the underlying disk continuum, forming the "local" continuum emission (see Mejía-Restrepo et al. 2016 for a detailed discussion).

From each fitted emission-line profile, we extract (1) the shift of the line centroid, i.e., the flux-weighted average center of the line emission and (2) the shift of the line peak—providing two probes of Δv; (3) the total line luminosity; and (4) the line width, in terms of the FWHM. From the latter, we subtract in quadrature the instrumental spectral resolution, according to the observational setup (i.e., in velocity space; see Koss et al. 2022a, 2022b). Whenever the resolution-corrected FWHMs of narrow lines fall below the corresponding instrumental resolution, we regard the emission-line FWHMs as upper limits and report the (velocity-equivalent) instrumental resolution in our catalog (see descriptions in Tables 5–8). We note that even in these cases (affecting 26 sources with Hβ measurements and 69 sources with Hα measurements), the narrow lines still provide the best way to decompose the complex key broad-emission-line profiles and tease out the broad-emission-line widths, which are crucial for BH mass estimates.

Together with the line-profile properties, we also computed the monochromatic continuum luminosities at several narrow wavelength bands, $L_\lambda \equiv \lambda\, L(\lambda)$, to be used for the estimation of $M_{\rm BH}$. In particular, we measured L_{1450}, L_{3000}, L_{5100}, and L_{6200} for $M_{\rm BH}$ estimates using C IV, Mg II, Hβ, and Hα, respectively (see, e.g., Greene & Ho 2005; Vestergaard & Peterson 2006; Wang et al. 2009; Mejía-Restrepo et al. 2016).

Uncertainties on all spectral measurements were derived by a resampling procedure. Each observed spectrum was used to generate 100 mock spectra, based on its noise (variance). Each of these mock spectra was then fit using our spectral decomposition procedures. For each measured quantity, of each AGN, the 16th and 84th percentiles of the corresponding distribution of measurements were then used to determine the corresponding uncertainty.

All spectral fits were visually inspected by at least three independent, experienced team members (J.M.-R., B.T., and M.K.). In the cases where the fits were inadequate, we have adjusted some of the parameters of the fitting procedure and refitted the data. These manual adjustments typically involved the continuum placement and/or the limits to the widths and/or shifts of emission-line components. We note that these minor numerical adjustments did not contradict the physical motivation and/or meaning of the emission components (e.g., broad Gaussian components always remained broader than the narrow ones, etc.).

We ultimately visually inspected all the final (adjusted) spectral fits, used them to derive the spectral measurements we rely upon throughout the rest of the paper and catalog (as well as the related uncertainties, using our resampling procedure), and assigned them spectral fit-quality flags, which we describe immediately below.

2.3. Model Fit Quality

We visually inspected all the (final) spectral fits and assigned a quality flag ($f_{\rm Q}$) representing the quality of each fit (i.e., each spectral complex for each source), ranging from 1 to 3. $f_{\rm Q} = 1$ marks good quality fits, with randomly distributed residuals, providing the most reliable line measurements we can hope to achieve within the scope of a large effort like BASS. $f_{\rm Q} = 2$ is used to mark good/acceptable fits, which may show slight systematic residuals and that could be slightly improved with further, less-trivial manual adjustments; however, $f_{\rm Q} = 2$ fits can still be used to provide reliable broad-line measurements. In such cases, we preferred not to further adjust the fits, as this may make our fitting procedure too heterogeneous. Finally, $f_{\rm Q} = 3$ marks those spectral fits that have failed and/or data that exhibit very low signal-to-noise or otherwise severe issues. In such cases, our (reasonable) attempts to manually adjust the spectral fitting procedure could not result in an acceptable fit. We exclude all such $f_{\rm Q} = 3$ fits from both the BASS/DR2 catalog and any of the analysis that follows. We further discuss these problematic fits in Section 2.3.1 below.

Examples of spectra and best-fit models representing the three $f_{\rm Q}$ classes are shown in Appendix A and Figure 13. By examining the results of the "useful" fits (i.e., with $f_{\rm Q} = 1$ and 2), we estimate that the minimum rest-frame equivalent width (rEW) needed to achieve such high-quality fits for the Hα, Hβ, Mg II, and C IV lines are EW = 10, 3, 9, and 10 Å, respectively.[33]

Out of the initial 515 and 433 unique objects with available spectra of the broad Hα and/or Hβ lines (respectively), after retaining only fits with $f_{\rm Q} = 1$ and 2, we end up with 457 unique AGNs with useful measurements of the broad Hα line, of which 341 and 77 unique objects have $f_{\rm Q} = 1$ and 2 (respectively), and 381 AGNs with useful measurements of the broad Hβ line, of which 245 and 118 unique objects have $f_{\rm Q} = 1$ and 2 (respectively). The remaining useful measurements come from sources with acceptable fits but large errors ($f_{\rm Q} = 2.5$; see Section 2.3.1 below). Also, there are 348 AGNs for which we have useful measurements of both the Hβ and Hα broad emission lines. In total, we have 485 unique AGNs with useful measurements of either the Hα and/or Hβ broad emission lines. For higher-redshift sources ($z \gtrsim 0.7$), essentially all of which are classified as beamed AGNs, only the Mg II and/or the C IV lines are available in our optical spectroscopy.

[33] Given the highly heterogeneous nature of the BASS/DR2 spectroscopic observations and data, we prefer to report the lowest EWs (i.e., physically weakest lines) we can measure, instead of reporting a more generic S/N criterion.

Table 2
Breakdown of Failed and/or Problematic Spectral Fits

Reason for Failure	Hα	Hβ	Mg II	C IV	Total Spectra
Low S/N	15	18	8	4	45
Tellurics	7	0	1	0	8
Unclear BLR	0	1	0	0	1
Mismatched NLR	2	0	0	0	2
Incomplete profile	3	1	0	2	6
Reduction issue[a]	2	9	4	2	17
Fe II fit issue	0	2	0	0	2
Absorption features[b]	0	1	0	2	3
Double-peak broad lines	29	20	0	0	49
Total failed fits	58	52	13	10	133

Notes.
[a] This includes fringing (or otherwise "wavy" spectral features), problems with flux calibration, and other artifacts.
[b] Indicating a strong absorption feature superimposed on the (broad) emission line, which limits our ability to properly model the latter.

From the initial 41 and 32 spectra with broad Mg II and C IV lines (respectively), we obtained 28 and 22 useful measurements of the Mg II and C IV broad-emission-line complexes (respectively). These are further split into 15 and 13 fits with $f_Q = 1$, and 13 and 9 fits with $f_Q = 2$ (in each case, for Mg II and C IV, respectively). There are six objects with useful measurements in both Mg II and C IV. Our data set thus consists of 43 unique AGNs with either Mg II and/or C IV broad-line measurements, out of which 27 do not have complementary Hα and/or Hβ broad-line measurements. Therefore, we end up with a total of 512 objects (485, from Hα and Hβ, plus 27, from Mg II and C IV) with BH mass estimations from broad emission lines.

2.3.1. Problematic Fits

After our visual inspection of the spectral fits (including those that required minor adjustments), we have a total of 29 objects with failed fits ($f_Q = 3$) of the broad Hα line, 32 in the case of Hβ, 13 in the case of Mg II, and 10 in the case of C IV. There is a variety of reasons for such failed fits, including a low signal-to-noise ratio (S/N), imperfect correction of telluric features associated with certain redshift ranges, incomplete profiles due to the specific source redshift and observation setup, and/or difficulties in data reduction. Table 2 summarizes the breakdown of the failed fits according to these (and other) categories, and below we further discuss some of the main ones.

Among the 15 objects with low S/N over the Hα complex, 4 are classified as Type 1.9 AGNs, that is, sources that show broad Hα but no broad Hβ line emission (see Section 3.1 for more details). This may result from significant obscuration by dust, dimming even the Hα emission and making even prominent emission lines like Hα harder to detect and model. There are also two beamed ("BZQ") AGNs whose Hα line is difficult to detect due to their relatively high redshift. The remaining systems with low S/N are bona fide broad-line (Type 1) AGNs whose spectra have not been reobserved since DR1, despite their apparent low S/N in that initial data release. The higher number of objects with low S/N in the Hβ line, 18, is not surprising as Hβ is weaker than Hα by at least a factor of ∼3 and thus requires a higher overall S/N, particularly given the need to properly model the blended iron emission complex. These low-S/N sources will likely be reobserved in future BASS spectroscopy and analyzed as part of a future DR.

For one source (BAT ID 1204, a.k.a. RBS 2043), the Mg II emission line is considerably narrower (≈1200 km s^{-1}) than what is seen in quasars, while the Hβ line is narrower still, consistent with an NLR origin. The Mg II width leads to a BH mass estimate (see Section 2.4 below) that is much lower than what is deduced from stellar velocity dispersion ($\log [M_{BH}/M_\odot] \simeq 7.4$ versus 9.6; Koss et al. 2022c). Our broad-line catalog thus reports the basic measurements for the Mg II spectral complex but not the associated BH mass.

There is a single object with an unclear presence of BLR features (in Hβ; BAT ID 349, a.k.a. UGC 3601), that is, with the data in hand we could not robustly determine whether there is a broad-emission component. We note that, in principle, in extreme cases, one could also expect a misidentification of blended narrow Hα and [N II] lines as a broad and weak Hα profile. We have not identified such questionable broad Hα profiles among our BASS/DR2 AGNs. At any rate, if such ambiguous cases indeed have broad Balmer emission lines (that is, they originate from the BLR), their measurement would require sufficiently high S/N and line EW, as well as a more detailed analysis (see, e.g., Oh et al. 2015 for detailed examples and discussion).

In addition to the failed fits (i.e., $f_Q = 3$), our inspection of the fitting results uncovered another subset of 57 spectral fits for which the resampling technique resulted in exceptionally large (fractional) uncertainties on the Hα (39 sources) and/or Hβ (18 sources) line widths, $\Delta[\mathrm{FWHM}]/\mathrm{FWHM} \geqslant 50\%$, and/or large systemic offsets of the narrow lines. However, our visual inspection suggests the fits are acceptable. Upon closer inspection, it seems that in these cases, the contrast between the broad emission line and the adjacent continuum emission is relatively low, which led a significant fraction of the resampled (mock) spectra to be fitted by extremely broad profiles (i.e., FWHM > 10,000 km s^{-1}). Because the best-fit parameters appear to represent the observed spectra well, we do not downgrade the quality flags of such fits to $f_Q = 3$, and instead mark these 43 cases with a dedicated flag, $f_Q = 2.5$.

We finally note that any physical interpretation of the line (velocity) shifts reported in our catalog should be done with care, as these naturally depend on the precise redshifts used for our spectral analysis. Specifically, any interpretation of narrow-emission-line shifts should consider the fact that our redshifts are, themselves, based on narrow emission lines (i.e., [O III] λ5007; Koss et al. 2022b). The two sources in our catalog that have extremely large shifts listed (>1000 km s^{-1}; BAT IDs 334 and 1332) are also marked as $f_Q = 2.5$.

To summarize, users of our catalog who prefer to have the largest possible sample of reliable fits of broad emission lines, and of derived quantities, can use the default quality cut $f_Q < 3$. More cautious analyses may however prefer to impose the stricter $f_Q \leqslant 2$ cut. We indeed adopt this stricter cut for all of the analyses presented below.

In addition to the failed fits described above, we also excluded from our main catalog and analysis objects with indications of double-peaked broad emission lines where the SE BH mass estimation approach is not applicable, and their physical origin is still debated. The proposed origins of such double-peaked line profiles include the accretion disk, dual BLR in a binary SMBH system, bipolar outflows, and/or flares

Table 3
Parameters of Virial BH Mass Prescriptions

Observables	$\log K$	α	β
FWHM(Hα), L(bHα)	7.526	0.55	2.06
FWHM(Hβ), L_{5100}	6.721	0.65	2.00
FWHM(Mg II), L_{3000}	6.906	0.61	2.00
FWHM(C IV),L_{1450}	6.331	0.60	2.00

Note. The mass prescriptions are of the form $M_{\rm BH} = K\ (\lambda L_\lambda)^\alpha\ {\rm FWHM}^\beta$, with λL_λ in units of 10^{44} erg s^{-1}, FWHM in units of 1000 km s^{-1}, and $M_{\rm BH}$ in units of $M_\odot$.

or spiral arms in the accretion disk (see, e.g., Veilleux & Zheng 1991; Zheng et al. 1991; Eracleous & Halpern 1994; Jovanović et al. 2010; Storchi-Bergmann et al. 2017; Ricci & Steiner 2019, and references therein). Out of our initial sample of broad-lined Swift/BAT AGNs, we find a total of 29 candidate double-peaked systems, comprising 29 and 20 sources with double-peaked Hα and Hβ, respectively (20 sources have double-peaked profiles in both Balmer lines). We provide basic information regarding these double-peaked sources in Table 4.

2.4. Black Hole Mass and Eddington Ratio Estimates

BH masses are estimated using the Hα, Hβ, Mg II, and C IV emission-line measurements, according to their availability for each source. In all our estimates, we assume a common (and universal) virial factor of $f = 1$.[34] This value is appropriate for $M_{\rm BH}$ estimates that rely on the FWHM of broad emission lines as the BLR velocity tracer and is further motivated by the observationally derived mean value from Woo et al. (2015), where RM-based $M_{\rm BH}$ estimates were matched, on average, to the corresponding expectations from the $M_{\rm BH}$–$\sigma_\star$ relation. Woo et al. (2015) found an uncertainty on the mean value of f of about 30%.

For the Hα line, we used the specific prescription calibrated in Greene & Ho (2005), in particular their Equation (6). We note, however, that their calibration assumed $f = 0.75$ (corresponding to a spherical BLR distribution). Our choice of $f = 1$ therefore requires adjusting the Greene & Ho (2005) calibration by $\times 4/3$ (or $+0.125$ dex). Our Hα-based prescription for $M_{\rm BH}$ is thus

$$M_{\rm BH}({\rm H}\alpha) = 2.67 \times 10^6 \times \left(\frac{L[{\rm bH}\alpha]}{10^{42}\ {\rm erg\ s^{-1}}}\right)^{0.55} \left(\frac{{\rm FWHM[bH}\alpha]}{10^3\ {\rm km\ s^{-1}}}\right)^{2.06} M_\odot. \quad (2)$$

We note that this prescription was calibrated to best match Hβ-related (RM) measurements, and it does not strictly follow the virial assumption, in the sense that the exponent of the velocity term is 2.06 (and not 2.00). In the case of Hβ, we used the calibration presented in Trakhtenbrot & Netzer (2012) while in the case of Mg II and C IV we followed Mejía-Restrepo et al. (2016). A summary of the specific calibrations that we adopted can be found in Table 3.

While not essential for the main findings of the present study, we use two key properties of broad-line AGNs to provide context in Section 3: their bolometric luminosities, $L_{\rm bol}$, and Eddington ratios, $L/L_{\rm Edd} \equiv L_{\rm bol}/(1.5 \times 10^{38} M_{\rm BH})$. This scaling assumes $L_{\rm bol}$ in units of erg s^{-1}, $M_{\rm BH}$ in units of $M_\odot$, and solar composition gas. For $L_{\rm bol}$ estimates, we rely on the intrinsic, absorption-corrected X-ray luminosities in the 2–10 keV regime, $L_{\rm int}$(2–10 kev), as determined through the elaborate spectral decomposition of the entire X-ray SEDs, discussed in detail in Ricci et al. (2017a). We then assume a simple, universal bolometric correction of $\kappa_{\rm 2-10\ kev} \equiv L_{\rm bol}/L_{\rm int}(2\text{–}10\ {\rm kev}) = 20$, which is a typical value for luminous AGNs (e.g., Marconi et al. 2004; Vasudevan et al. 2009). There are many other bolometric corrections suggested in the literature, including those defined at other spectral regimes (e.g., Richards et al. 2006; Runnoe et al. 2012; Trakhtenbrot & Netzer 2012), luminosity-dependent corrections (e.g., Marconi et al. 2004; Trakhtenbrot & Netzer 2012; Duras et al. 2020), $L/L_{\rm Edd}$-dependent ones (e.g., Vasudevan et al. 2009), and/or those motivated by accretion-disk models (e.g., Netzer 2019). To exemplify how these various prescriptions may affect the simple $L/L_{\rm Edd}$ estimates we use here, we note that given the range of $L_{\rm int}$(2–10 kev) for our broad-line sources, the luminosity-dependent prescription of Marconi et al. (2004) would suggest $\kappa_{\rm 2-10\ kev} \sim 10$–70.

The publicly available DR2 catalogs provide many measurements that can be used for alternative determinations of $L_{\rm bol}$ (and thus of $L/L_{\rm Edd}$), and in particular rest-frame optical monochromatic continuum luminosities (L_{5100}) and broad Hα line luminosities (L(bHα); both included in this catalog[35]), as well as X-ray continuum luminosities ($L_{\rm 2-10\ keV}$ and $L_{\rm 14-150\ keV}$). Indeed, other BASS (DR2) publications may use different choices for the determination of $L_{\rm bol}$ and $L/L_{\rm Edd}$, as best suits their science goals.

We finally stress that neither the $M_{\rm BH}$ nor the $L_{\rm bol}$ prescriptions we use were calibrated using, or are meant to be applied on, beamed AGNs. In such sources, the continuum X-ray, UV, and optical luminosities may be boosted, and thus both $M_{\rm BH}$ and $L_{\rm bol}$ may be significantly overestimated. We describe the identification of beamed sources among our sample of BASS/DR2 broad-line AGNs in Section 3.1.

3. The BASS/DR2 Broad-line Catalog

In this section we present the BASS/DR2 broad-emission-line catalog and some key characteristics of the broad-line AGN demographics in BASS.

Our detailed spectral measurements, their uncertainties, and select derived quantities are provided in machine-readable form herein and online.[36] Tables 5, 6, 7, and 8 (in Appendix D) describe the content of the BASS/DR2 broad-line catalogs for the Hα, Hβ, Mg II, and C IV spectral regions (respectively) for the BASS/DR2 AGNs with adequate spectral fit quality ($f_{\rm Q} < 3$). We also provide, in a separate set of tables with identical format, spectral measurements for the 177 AGNs from the "bonus" sample (i.e., sources drawn from deeper-than-70 months Swift/BAT survey data), which had adequate spectral fit quality (i.e., $f_{\rm Q} \leqslant 2$).

In Appendix B we provide a detailed comparison of line-width and BH mass measurements derived in BASS/DR2 and DR1 for those broad-line AGNs that are part of both DRs.

[34] This virial factor is appropriate for $M_{\rm BH}$ prescriptions that depend on the FWHM of the respective emission line and corresponds to $f_\sigma = 5.5$ if one uses line velocity dispersion instead (for a single Gaussian profile).

[35] The luminosities measured in the optical regime are corrected for galactic extinction.

[36] http://www.bass-survey.com/data.html

Figure 14 summarizes these comparisons graphically, highlighting that our DR2 spectral measurements are, overall, in excellent agreement with DR1 measurements.

3.1. Demographics of Optical AGN Emission-line Classes

Here we further refine the classification of broad-line AGNs in BASS/DR2, with coverage of both Hβ and Hα, based on the presence and (relative) strength of the broad components of these emission lines (e.g., Osterbrock 1981). Specifically, we follow the quantitative approach outlined in Winkler (1992) to classify our sources into AGN subclasses (Types 1, 1.2, 1.5, 1.8, 1.9, and 2) using the observed flux ratio of the broad Hβ to the [O III] emission lines, $L(\mathrm{bH}\beta)/L([\mathrm{O\ III}])$, as follows:

1. Sy1 if $L(\mathrm{bH}\beta)/L([\mathrm{O\ III}]) > 5.0$;
2. Sy1.2 if $2.0 < L(\mathrm{bH}\beta)/L([\mathrm{O\ III}]) < 5.0$;
3. Sy1.5 if $1/3 < L(\mathrm{bH}\beta)/L([\mathrm{O\ III}]) < 2.0$;
4. Sy1.8 if $L(\mathrm{bH}\beta)/L([\mathrm{O\ III}]) < 1/3$; broad component visible in both Hα and Hβ;
5. Sy1.9 if there is a broad component visible in Hα but not in Hβ.
6. Sy2 if no broad components are visible.

Throughout the rest of this work, we refer to "Type 1.x" AGNs simply as "Sy1.x" sources. This "Sy" nomenclature is used here for the sake of simplicity and consistency with previous work, despite the fact that many of our BASS/DR2 AGNs may not be considered as "Seyfert galaxies" given their high (X-ray) luminosities.

We acknowledge that this classification scheme practically depends on source distance (or redshift), as it combines aperture-limited measurements of the compact, unresolved BLR (broad Balmer lines) and of the extended, host-wide [O III] emission. Thus, for any given slit width and/or angular extraction aperture and a given (intrinsic) $L(\mathrm{bH}\beta)/L([\mathrm{O\ III}])$, the measured [O III] flux would increase and thus the $L(\mathrm{bH}\beta)/L([\mathrm{O\ III}])$ ratio would decrease, with increasing source distance (redshift). This may systematically shift the classification of sources toward weaker broad components or more specifically shift the classification of a source from, e.g., Sy1 to Sy1.2 or from Sy1.2 to Sy1.5. We stress, however, that the present study focuses on the comparison between Type 1.9 AGNs (Sy1.9s) and the combined group of Types 1, 1.2, and 1.5 AGNs (Sy1–1.5s). Consequently, this caveat does not affect our key results. Additionally, whenever we present separate results for Sy1, Sy1.2, and Sy1.5 sources, we verify that the quoted statistics of each AGN type subsample (i.e., medians and/or means) are not statistically different from each other. More generally, the interested reader is encouraged to use the tabulated slit/aperture widths of all BASS/DR2 optical spectra, and the distances to all AGNs, to address this caveat in any future study that relies on BASS data (details are available in Koss et al. 2022b).

A previous BASS study by Shimizu et al. (2018) investigated Sy1.9 sources in BASS/DR1 and showed that Sy1.9s with high column densities, i.e., $\log(N_{\mathrm{H}}/\mathrm{cm}^{-2}) > 22$ and especially galaxies with $\log(N_{\mathrm{H}}/\mathrm{cm}^{-2}) \gtrsim 23$, have optical spectra that may be contaminated by line emission from outflowing gas. Such systems have broad Hα lines that are relatively narrow and that are blueshifted with respect to the NLR emission, as well as outflow signatures in their [O III] profiles. That study was based on ad hoc emission-line diagnostics that were motivated by spatially resolved (IFU) data for certain exemplary systems and further noted that with higher-resolution spectroscopy, these misclassified outflowing systems would be easy to identify. The superior BASS/DR2 data we use here, with hundreds of new VLT/X-Shooter spectra, indeed allow us to more directly rule out the possibility that outflows dominate the key emission-line complexes considered in the present study and to be more confident in our classification of (high-N_{H}) Sy1.9 systems in BASS/DR2. We thus proceed with our analysis of all BASS/DR2 AGNs, including Sy1.9 sources, according to the criteria listed above. We defer the identification of (weak) outflow signatures in such sources to a future study.

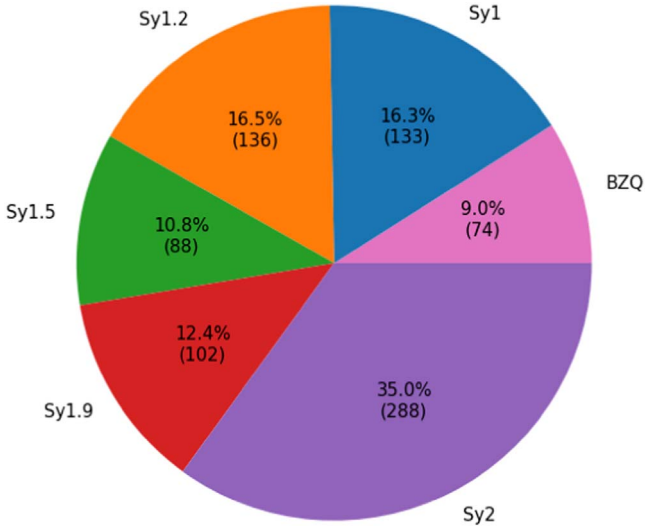

Figure 1. The distribution of BASS/DR2 AGNs in terms of various AGN type subclasses. We show the percentages and total numbers of Sy1 (blue), Sy1.2 (orange), Sy1.5 (green), Sy1.9 (red), Sy2 (purple), and BZQ (magenta) sources. See text for classification details.

In addition to the AGN subclassification, we also mark in our catalog the 67 beamed AGNs, comprised of high-z systems and "candidate" beamed sources, with a dedicated flag (BZQ). These are blazars or flat-spectrum radio quasars, where Doppler boosting may significantly amplify the nonthermal emission of the central engine, including the hard X-rays. This classification was done based on commonly used techniques (e.g., intense radio emission, a flat radio spectrum, dramatic variability), combined with cross-matching to Fermi data products and multiwavelength broadband SED fitting (e.g., Oh et al. 2018; Paliya et al. 2019). The BASS/DR2 Data & Catalog paper (Koss et al. 2022b) provides further information on the classification of these sources, particularly those not identified as beamed AGNs in BASS/DR1 (see Paliya et al. 2019 and L. Marcotulli et al., in preparation). This identification of beamed AGNs eventually included all AGNs with (reliable) measurements of the Mg II and/or C IV broad emission lines (i.e., $z \gtrsim 0.43$ and $\gtrsim 3.67$, respectively). There are also 22 (candidate) beamed systems among the lower-z sources, where our optical spectra cover the spectral complexes of Hβ and/or Hα. Our catalog provides all the available spectral measurements and derived properties (including AGN type subclasses when possible), regardless of any evidence for beaming. We note that continuum and line measurements for such sources should be used with caution, while line ratios may be more robust.

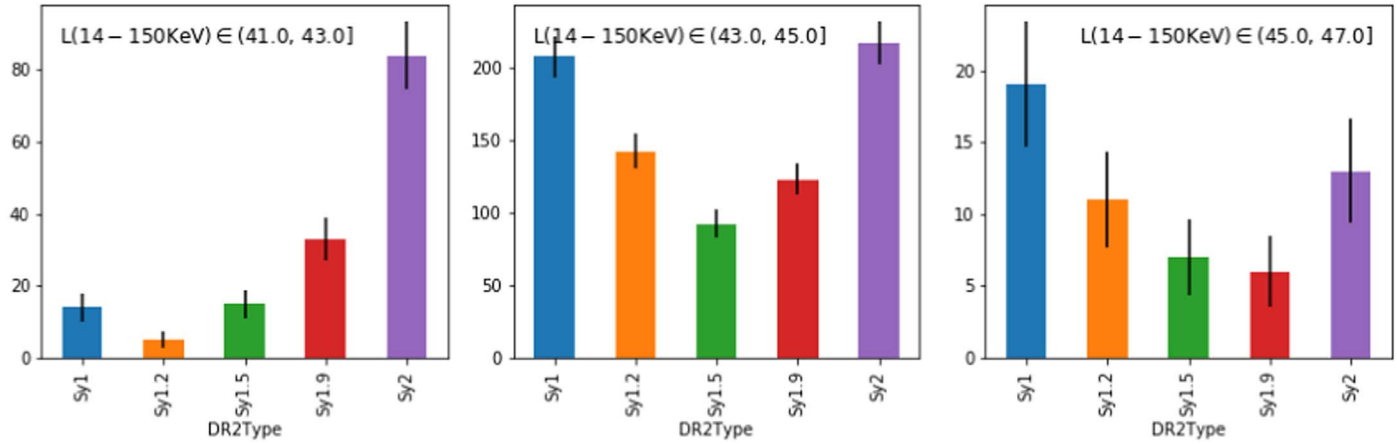

Figure 2. The distribution of BASS/DR2 AGNs among AGN type subclasses in bins of ultrahard X-ray luminosity ($\log L_{14-150\,\mathrm{keV}}$), as indicated in each panel. Higher (lower) luminosity AGNs tend to preferentially belong to the Sy1–1.2 (Sy1.9–2) classes.

In Figure 1 we show the composition of our BASS/DR2 sample of broad-line AGNs in terms of the fraction and total number of sources belonging to each of the aforementioned AGN Type subclasses (Sy1.0, 1.2, 1.5, 1.9, and BZQ). We do not identify any Sy1.8 sources among our BASS/DR2 AGNs. For completeness, we also include narrow-line BASS/DR2 AGNs (Sy2s), which are not part of the present catalog and are instead presented in other BASS/DR2 papers (Koss et al. 2022a, 2022b; Oh et al. 2022).

In Figures 2 and 3 we further illustrate how the fractions of AGNs in each of the AGN subclasses vary with (ultrahard) X-ray luminosity. At low luminosities ($L_{14-150\,\mathrm{keV}} < 10^{43}\,\mathrm{erg\,s^{-1}}$), the population is mostly dominated by Sy2 and Sy1.9 sources; however, as the X-ray luminosity increases, the relative fraction of Sy1–1.5 sources increases, while the fraction of Sy1.9s and Sy2s decreases. This trend is in agreement with several previous studies (e.g., Lawrence 1991; Maiolino et al. 2007; Merloni et al. 2014; Oh et al. 2015; Ricci et al. 2017b; Ichikawa et al. 2019), which suggest that the typical dust-covering factor in AGNs decreases as the radiative power of the accretion disk increases. Earlier studies attributed this trend to the "receding torus" scenario, where the increasing (UV) disk emission sublimates dust at increasingly larger (inner) radii of the dusty torus. A previous BASS study by Ricci et al. (2017b) conclusively showed that the underlying trend is in fact that the fraction of unobscured sources increases with increasing L/L_{Edd} (and not L). The dearth of high-L/L_{Edd}, high-N_{H} AGNs is commonly interpreted as evidence for the amount of obscuring material, and indeed the degree of obscuration, to be driven by radiation pressure exerted by the central engine on the (inner) obscuring toroidal structure (e.g., Fabian et al. 2009; Ricci et al. 2017b; Ishibashi et al. 2018, and references therein). Revisiting the distribution of BASS/DR2 AGNs in the L/L_{Edd}–N_{H} plane, and the relevant physical scenarios, is beyond the scope of the present study and will be addressed in a forthcoming BASS publication (see, however, the results of the companion BASS/DR2 paper by Ananna et al. 2022).

We note that selection effects may also play a role in the trends seen in Figures 2 and 3. For instance, as the accretion-disk luminosity decreases, the contrast of the AGN with respect to the host galaxy also decreases. In the context of BASS optical spectroscopy, the S/N required to robustly detect broad emission lines would become unrealistically large, and our analysis may thus favor the classification of low-luminosity AGNs as Sy2 and Sy1.9 sources, over the Sy1–1.5 subclasses.

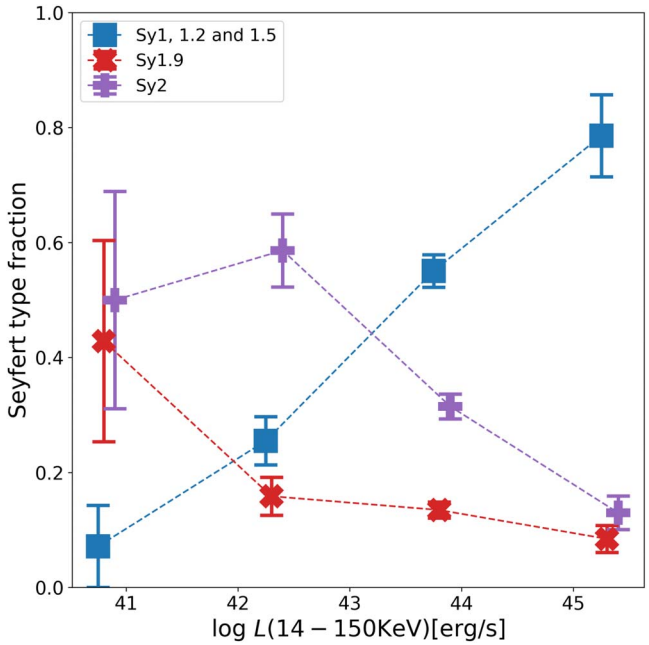

Figure 3. The fraction of BASS/DR2 AGNs of various AGN type subclasses as a function of ultrahard X-ray luminosity ($\log L_{14-150\,\mathrm{keV}}$). The various symbols and lines trace AGNs belonging to the Sy1–1.5 (blue), Sy1.9 (red), and Sy2 (purple) subclasses.

3.2. Comparison of Hα and Hβ Line-width and M_{BH} Measurements

In Figure 4 we compare the FWHM measurements (left panel) and M_{BH} estimates (right panel) associated with the broad Hβ and Hα emission lines. Our FWHM(Hα) and FWHM(Hβ) measurements are generally in good agreement with the relation derived by Greene & Ho (2005; see the red dashed–dotted line). A formal fit to our set of FWHM measurements, derived using the `emcee` Markov Chain Monte Carlo (MCMC) sampler (Foreman-Mackey et al. 2013), yields

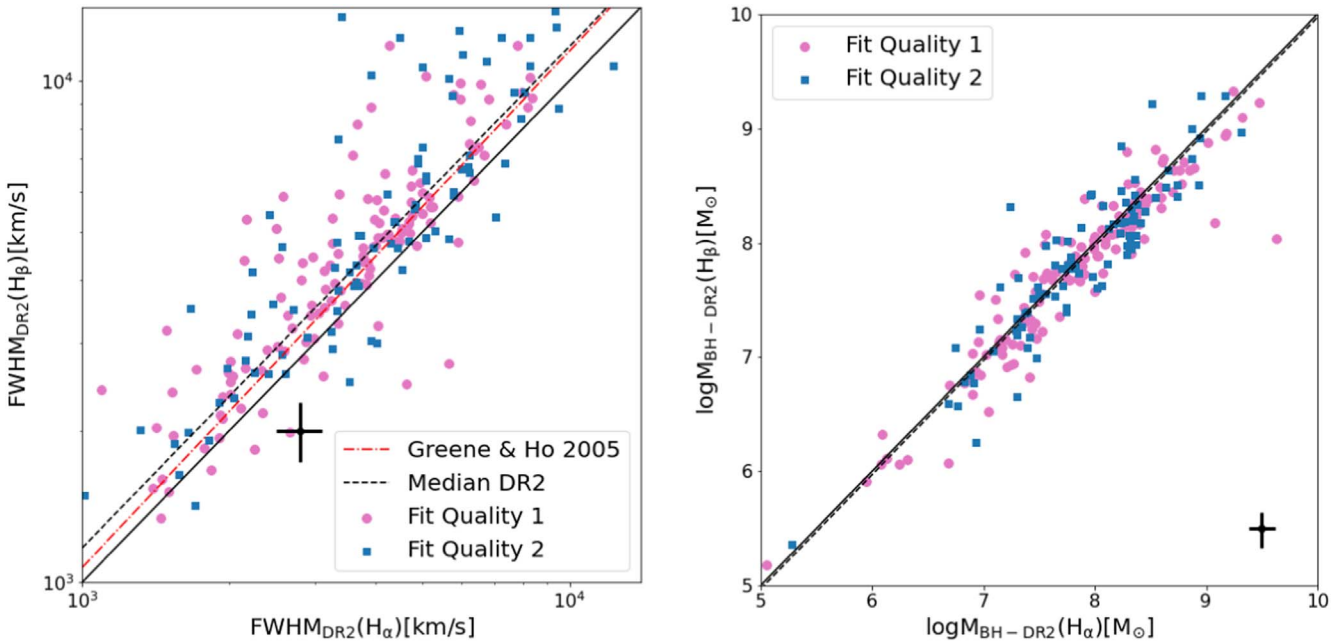

Figure 4. Hβ vs. Hα FWHMs (left) and BH masses (right) in BASS/DR2. Black solid crosses represent the median error bars associated with the FWHM and $M_{\rm BH}$ estimates. The relation we find between FWHM(Hα) and FWHM(Hβ) (black dotted line) is broadly consistent with the relation derived in Greene & Ho (2005, red dotted line), which supports our use of their Hα-based $M_{\rm BH}$ prescription. The black solid line represents the 1:1 relation.

the best-fit relation

$$\log \mathrm{FWHM(H}\beta) = (0.98 \pm 0.05)\log \mathrm{FWHM(H}\alpha) + (0.16^{+0.19}_{-0.17}), \quad (3)$$

where FWHMs are given in km s^{-1}, and the quoted uncertainties represent 95% confidence intervals. A fit using the BCES(Y|X) method (Akritas & Bershady 1996) provides an indistinguishable best-fit relation.

The right panel of Figure 4 shows that our Hβ- and Hα-based $M_{\rm BH}$ estimates are indeed in excellent agreement, with a median offset of merely 0.03 dex and a scatter of 0.25 dex. This scatter is mostly driven by the scatter between FWHM(Hα) and FWHM(Hβ), which is found to be 0.11 dex, and therefore expected to yield a scatter of 0.23 dex in $M_{\rm BH}$. This agreement between Hβ- and Hα-based $M_{\rm BH}$ estimates further justifies our choice to use the not-strictly virial Hα-based $M_{\rm BH}$ prescription, derived by Greene & Ho (2005). We stress again that the excellent agreement between the two kinds of mass estimates is reached only after considering a virial factor of $f_{\rm FWHM} = 1$ for both the Hα and Hβ mass prescriptions. This is justified as the two lines are expected to be formed in a similar region within the BLR and consequently should have the same geometrical factor.

3.3. Black Hole Mass and Eddington Ratio Distributions

In Figure 5 we show the distribution of broad-line BASS/DR2 AGNs in the $M_{\rm BH}$–$L/L_{\rm Edd}$ plane, with sources further divided either by AGN subclass (top left) or by redshift ranges (top right). We also show the cumulative distributions of $L_{\rm bol}$ (bottom left), $M_{\rm BH}$ (bottom center), and $L/L_{\rm Edd}$ (bottom right). In this analysis, we include all AGNs for which reliable estimates of $M_{\rm BH}$ (and thus of $L/L_{\rm Edd}$) are derived from broad emission lines, that is, Types 1–1.9 AGNs, and beamed sources (BZQ).

Figure 5 clearly demonstrates the wide range in both $M_{\rm BH}$ and $L/L_{\rm Edd}$ that is sampled by BASS/DR2 AGNs. First, unbeamed AGNs where both broad Hβ and Hα lines are robustly detected (Sy1–1.5 s hereafter) cover $6 \lesssim \log(M_{\rm BH}/M_\odot) \lesssim 10$ and $-3 \lesssim \log L/L_{\rm Edd} \lesssim 1$. This is comparable to the distribution reported in BASS/DR1 (see Figure 16 in Koss et al. 2017).[37] Compared with other wide-field AGN surveys in the local universe where SE mass estimates were used (e.g., Greene & Ho 2007; Vestergaard & Osmer 2009; Schulze & Wisotzki 2010), BASS naturally includes the most-luminous, rarest AGNs accessible, powered by the most-massive and/or highest-$L/L_{\rm Edd}$ BHs.

Second, beamed AGNs in BASS/DR2, which preferentially reside at higher redshifts, appear to have higher $L_{\rm bol}$, $M_{\rm BH}$, and $L/L_{\rm Edd}$, covering $8 \lesssim \log(M_{\rm BH}/M_\odot) \lesssim 10$ and, importantly, $-1 \lesssim \log L/L_{\rm Edd} \lesssim 2$ and $46 \lesssim \log(L_{\rm bol}/\mathrm{erg\ s^{-1}}) \lesssim 49$. Although this may be partially attributed to the higher redshifts of the beamed sources (given the flux-limited nature of the Swift/BAT all-sky survey), we stress again that in such systems $L_{14-150\ \rm keV}$ is most likely overestimated, as their X-ray emission is affected by jets and is boosted by relativistic effects. This propagates to an overestimated $L_{\rm bol}$ and thus $L/L_{\rm Edd}$.

Finally, a large fraction of (unbeamed) Sy1.9 sources show lower masses, $\log(M_{\rm BH}/M_\odot) \lesssim 7$, and higher Eddington ratios, $\log L/L_{\rm Edd} \gtrsim -1$, compared to Sy1–1.5 sources, while covering a similar luminosity range. This difference, however, likely highlights a bias in this class. As we show in the next section, the Hα-based masses of Sy1.9s are underestimated, and their $L/L_{\rm Edd}$ are thus overestimated, likely due to the suppression of broad Hα emission, which we argue is linked to (partial) obscuration of the BLR by dust. The small arrows added to each Sy1.9 in the top panels of Figure 5 demonstrate how a

[37] For a few sources, BASS/DR1 measurements indicated exceptionally low $L/L_{\rm Edd}$ (i.e., $\log L/L_{\rm Edd} \lesssim -4$). The higher-quality DR2 data and measurements have corrected the $L/L_{\rm Edd}$ measurements of these outliers.

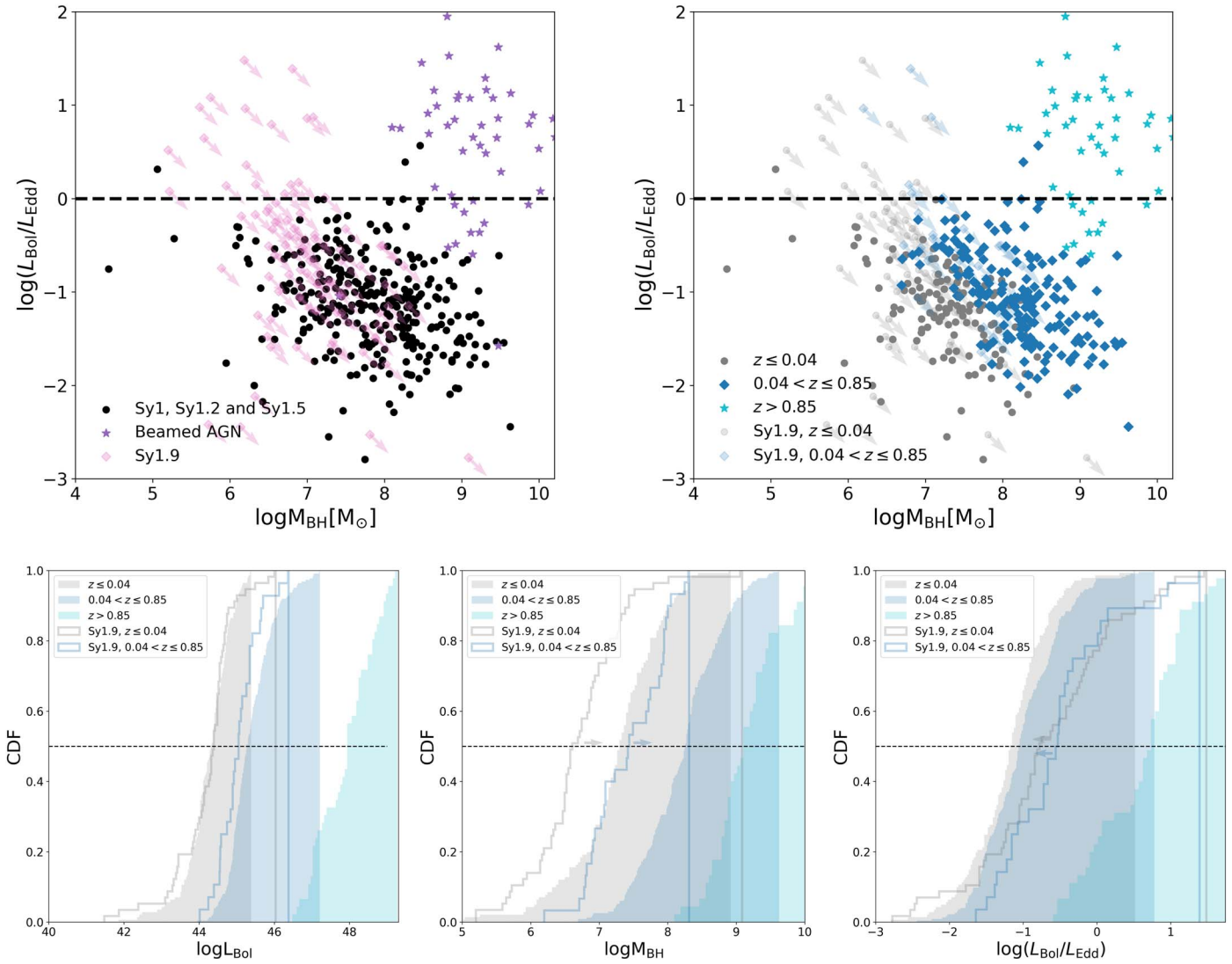

Figure 5. The luminosities, BH masses, and Eddington ratios of BASS/DR2 broad-line AGNs. Top: the distribution of BASS/DR2 AGNs in the $L/L_{\rm Edd}$–$M_{\rm BH}$ plane. Our AGNs are further split by AGN type (left panel) and by redshift range (right panel). Bottom: cumulative distributions of $L_{\rm bol}$ (left), $M_{\rm BH}$ (center) and $L/L_{\rm Edd}$ (right). The $M_{\rm BH}$ of Sy1.9 sources are likely underestimated, and their $L/L_{\rm Edd}$ are thus overestimated (see text for discussion). The small arrows in the top panels indicate the direction of a simple, uniform correction toward the true $M_{\rm BH}$ and $L/L_{\rm Edd}$ of Sy1.9s (see Section 4.5 for a more detailed discussion of mass corrections). The $L_{\rm bol}$ and $L/L_{\rm Edd}$ of beamed AGNs may be significantly overestimated due to jet emission and/or relativistic boosting.

simple (uniform) correction for this bias would be reflected in the $M_{\rm BH}$–$L/L_{\rm Edd}$ plane, with increasing $M_{\rm BH}$ and accordingly decreasing $L/L_{\rm Edd} \propto L/M_{\rm BH}$. In Section 4.5, we provide a set of simple $M_{\rm BH}$ corrections for Sy1.9 sources.

4. Reduced Broad Balmer Line Emission and Obscuration in BASS/DR2 AGNs

In what follows, we examine in detail the properties of the broad Balmer emission lines in our BASS/DR2 sample of broad-line AGNs. We particularly focus on those sources where only Hα but not Hβ broad-line emission is identified—i.e., Type 1.9 AGNs (Sy1.9s) and use the rich BASS data set to better understand these systems.

4.1. Preliminaries: Linking Broad Balmer Lines with X-Ray Measurements

As a first step, we look into the most basic links between the broad Balmer line measurements and the key properties deduced from the X-ray analysis of the BASS AGNs (Ricci et al. 2017a). Namely, we examine the observed links between (i) the broad Hα and ultrahard X-ray luminosities (L(bHα), $L_{14-150\,\rm keV}$), and (ii) the broad Balmer decrement (L(bHα)/L(bHβ), or simply Hα/Hβ in what follows) and the line-of-sight column densities ($N_{\rm H}$).

In Figure 6 we show L(bHα) versus $L_{14-150\,\rm keV}$ for the 434 nonbeamed AGNs with reliable broad Hα measurements in BASS/DR2, further highlighting the different AGN subclasses. Unsurprisingly, the two independently measured emission probes show a roughly uniform scaling for the vast majority of AGNs. However, for Sy1.9 sources, L(bHα) deviates downwards from the general scaling by roughly 0.8 dex. Thus, broad Hα emission seems to be suppressed in Sy1.9 sources relative to all other AGNs with detectable broad Hα emission (Sy1–1.5 sources) at any given $L_{14-150\,\rm keV}$. We note that this apparent suppression is not limited to particularly high- or low-luminosity sources (in terms of L(bHα) and/or $L_{14-150\,\rm keV}$). In the following section, we further investigate this suppression

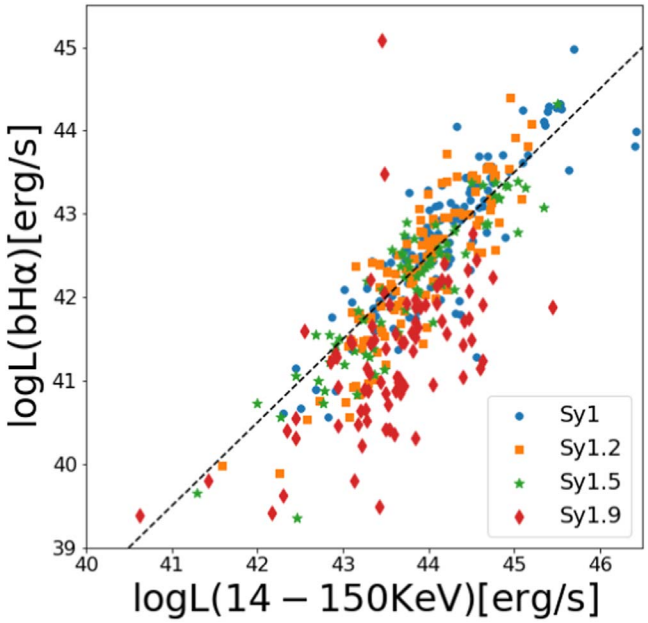

Figure 6. Broad Hα emission-line luminosity (L(bHα)) vs. ultrahard X-ray luminosity ($L_{14-150\,\mathrm{keV}}$) for BASS/DR2 AGNs. Symbol colors mark AGNs of different (emission line) subclasses, as indicated in the legend. The dashed line marks a scaling of $\log(L[\mathrm{bH}\alpha]/L_{14-150\,\mathrm{keV}}) = -1.5$, which describes the general trend seen in most of our bona fide broad-line AGNs. The broad Hα emission in Type 1.9 AGNs, however, appears suppressed relative to AGNs of other subclasses with comparable $L_{14-150\,\mathrm{keV}}$.

and how it may be linked to other basic AGN observables and properties.

When considering the measured decrements between the broad Hα and Hβ emission lines, we first note that close to 30% of the AGNs in our sample are Type 1.9 AGNs where the broad Hβ line cannot be detected and thus formally have $L(\mathrm{bH}\beta) = 0$ (and infinite Hα/Hβ). Deducing a robust upper limit on L(bHβ) (and thus a robust lower limit on Hα/Hβ) for such sources is challenging and requires a full spectral decomposition of the (stellar) host emission. In addition, about 40% of those sources with detectable broad Hβ show Hα/H$\beta > 3$, which—if taken at face value—may indicate significant attenuation over the Hβ wavelength regime, perhaps by dusty BLR gas (see, e.g., Dong et al. 2008; Baron et al. 2016, and references therein).

In Figure 7 we show the available Balmer decrement measurements for our sample, and how it varies with N_{H}. The left-hand-side panels show the distribution of Hα/Hβ for all the BASS/DR2 AGNs for which these quantities are robustly measured, i.e., omitting Type 1.9 AGNs. We further split our sample into AGNs with $\log(N_{\mathrm{H}}/\mathrm{cm}^{-2}) > 20$ and "completely unobscured" AGNs, which formally have $\log(N_{\mathrm{H}}/\mathrm{cm}^{-2}) = 20$ in the Ricci et al. (2017a) catalog. Note that this latter subsample includes sources with upper limits on N_{H}, so in practice, it covers $\log(N_{\mathrm{H}}/\mathrm{cm}^{-2}) \leqslant 20$ (see Ricci et al. 2017a for details). The right panel of Figure 7 shows Hα/Hβ versus N_{H} for broad-line BASS/DR2 AGNs with $\log(N_{\mathrm{H}}/\mathrm{cm}^{-2}) > 20$, again excluding Type 1.9 AGNs. All panels of Figure 7 also mark the canonical value of Hα/H$\beta = 2.87$, derived for Case B recombination in H II regions, as well as Hα/H$\beta = 3.1$ which is more relevant for AGNs. The latter is commonly adopted for the low-density NLR in AGNs and is also consistent with what is found for the broad Balmer lines (emitted from the high-density BLR) in large samples of optically selected quasars (see Dong et al. 2008 and references therein).

The median Balmer decrements for our subsamples of $\log(N_{\mathrm{H}}/\mathrm{cm}^{-2}) \leqslant 20$ and $\log(N_{\mathrm{H}}/\mathrm{cm}^{-2}) > 20$ AGNs are $\log$ (Hα/Hβ) = 0.52 and 0.58 (respectively), and the scatter measures (standard deviations) in Hα/Hβ for these two subsamples are 0.24 and 0.41 dex, respectively. The median Balmer decrements in our BASS/DR2 AGNs are in agreement with what is found for optically selected SDSS quasars (e.g., Dong et al. 2008, see reference lines in Figure 7). The scatter we find is higher than what is found for SDSS quasars (i.e., ∼0.05 dex; Dong et al. 2008). This is expected given that SDSS quasars are preselected based on their blue continuum colors, tracing unobscured accretion-disk emission (Richards et al. 2002), while our Swift/BAT-selected broad-line AGNs indeed cover a wider range of (circumnuclear) obscuration.

Among the $\log(N_{\mathrm{H}}/\mathrm{cm}^{-2}) > 20$ BASS/DR2 broad-line AGNs, there is a (mild) trend of increasing Balmer decrement with increasing column density, with a significant amount of scatter (right panel of Figure 7). This trend seems to involve objects of all subclasses (i.e., Sy1s, 1.2 s and 1.5s). A formal Spearman correlation test confirms that the correlation between L(bHα)/L(bHβ) and N_{H}, for all Sy1–1.8 AGNs with $\log(N_{\mathrm{H}}/\mathrm{cm}^{-2}) > 20$, is statistically significant but rather weak ($r_{\mathrm{s}} = 0.28$, $P_{\mathrm{s}} = 0.01$). Given the large scatter and the limited strength of the correlation, we refrain from fitting a formal relation that links L(bHα)/L(bHβ) and N_{H}.

The Balmer decrements we measure are far lower than what is expected from the corresponding column densities. For reference, for $\log(N_{\mathrm{H}}/\mathrm{cm}^{-2}) = 22$ one would expect a Balmer decrement of roughly Hα/H$\beta \simeq 17$, assuming a standard Galactic absorption scaling (i.e., gas-to-dust ratio; Bohlin et al. 1978) and a Cardelli et al. (1989) extinction law. This is barely consistent with the highest Hα/Hβ we measure for AGNs with comparable N_{H} (Figure 7, right). For higher N_{H}, the discrepancy grows substantially and quickly (expected Hα/H$\beta > 500$ by $\log(N_{\mathrm{H}}/\mathrm{cm}^{-2}) = 22.5$). This is consistent with several previous works, which found that the $E(B-V)/N_{\mathrm{H}}$ ratio in AGNs is lower than Galactic by a factor ranging from ∼3 and up to ∼100 (e.g., Maiolino et al. 2001a, 2001b), perhaps indicating that the material obscuring the central X-ray source is in part dust free (e.g., Burtscher et al. 2016). Alternatively, the X-ray-obscuring material may be arranged in a compact configuration, which does not (generally) affect the BLR radiation. The recent study by Jaffarian & Gaskell (2020) further discusses these and other scenarios to account for the differences between the levels of extinction deduced from Balmer line ratios and from (X-ray) hydrogen column densities. We will come back to this issue when discussing intermediate-type AGNs in Section 4.2.

4.2. Hα Line Attenuation in Partially Obscured AGNs

In Figure 8, we show L(bHα)/$L_{14-150\,\mathrm{keV}}$ (left) and L(bHβ)/$L_{14-150\,\mathrm{keV}}$ (right) versus $\log(N_{\mathrm{H}}/\mathrm{cm}^{-2})$ for our BASS/DR2 broad-line AGNs, with the respective distributions of these quantities (ancillary panels in each plot) and distinguishing the different AGN subclasses. The first thing to notice in Figure 8 is that Sy1.9 sources tend to have higher N_{H} than Sy1–1.5 sources. This difference is statistically significant, as confirmed by both Kolmogorov–Smirnov (KS) and Wilcoxon rank sum (WRS) tests. The P-values associated with the null hypotheses, i.e., the

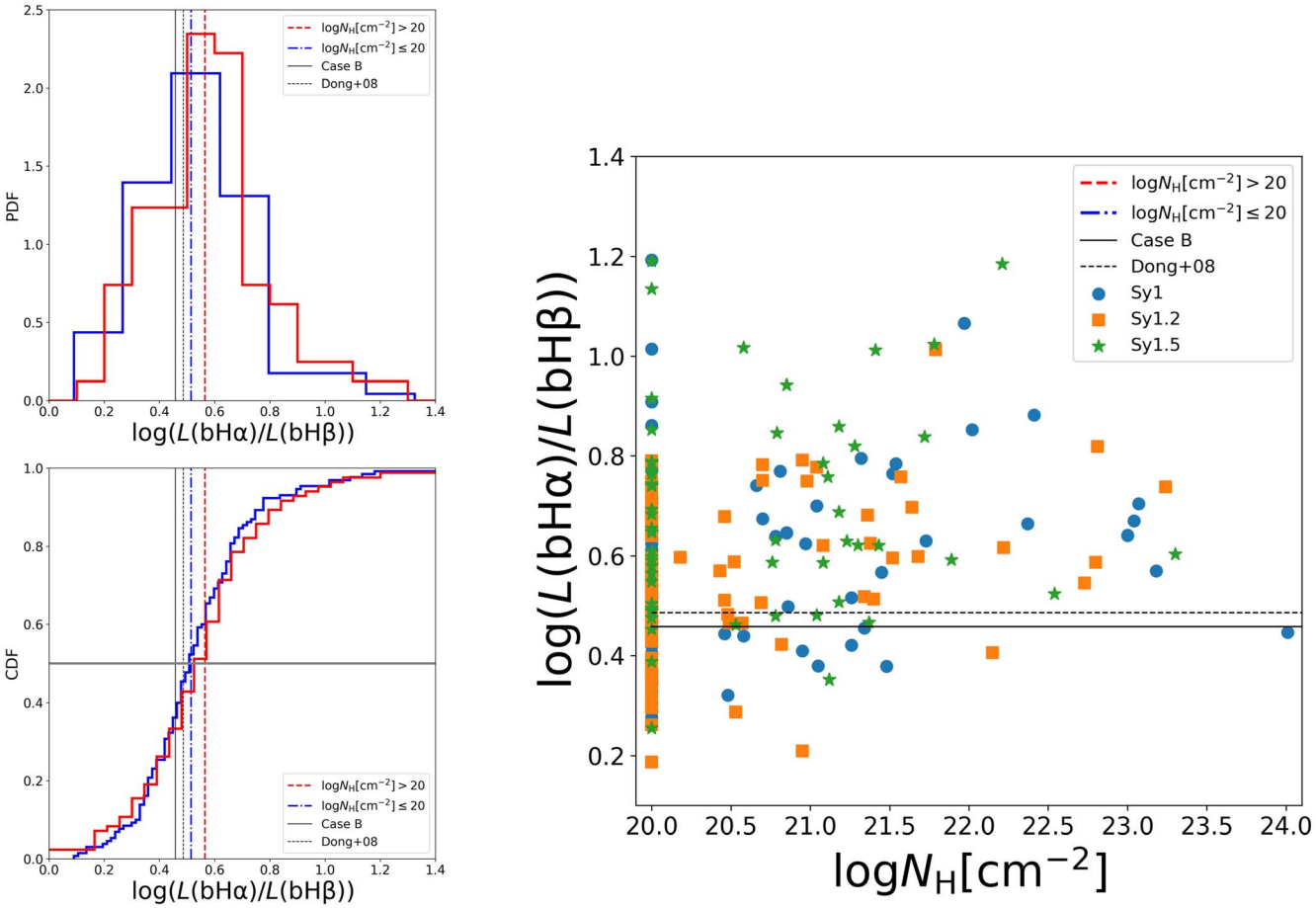

Figure 7. The Balmer decrement ($L(\mathrm{bH}\alpha)/L(\mathrm{bH}\beta)$) for broad-line BASS/DR2 AGNs. Left: the distribution of $\log(L(\mathrm{bH}\alpha)/L(\mathrm{bH}\beta))$ among unbeamed, broad-line BASS/DR2 AGNs, excluding Type 1.9 sources and further split into sources with $\log(N_\mathrm{H}/\mathrm{cm}^{-2}) > 20$ and $\log(N_\mathrm{H}/\mathrm{cm}^{-2}) \leqslant 20$ (top—probability distribution function; bottom—cumulative distribution function). Right: $\log(L(\mathrm{bH}\alpha)/L(\mathrm{bH}\beta))$ vs. $\log(N_\mathrm{H}/\mathrm{cm}^{-2})$ for AGNs with $\log(N_\mathrm{H}/\mathrm{cm}^{-2}) > 20$, again excluding Type 1.9 sources. Note the mild (yet statistically significant) positive correlation between the quantities. In all panels we mark the median values for the $\log(N_\mathrm{H}/\mathrm{cm}^{-2}) \leqslant 20$ (completely unobscured) and $\log(N_\mathrm{H}/\mathrm{cm}^{-2}) > 20$ subsamples, as well as two reference values from the literature (see legends and text for details).

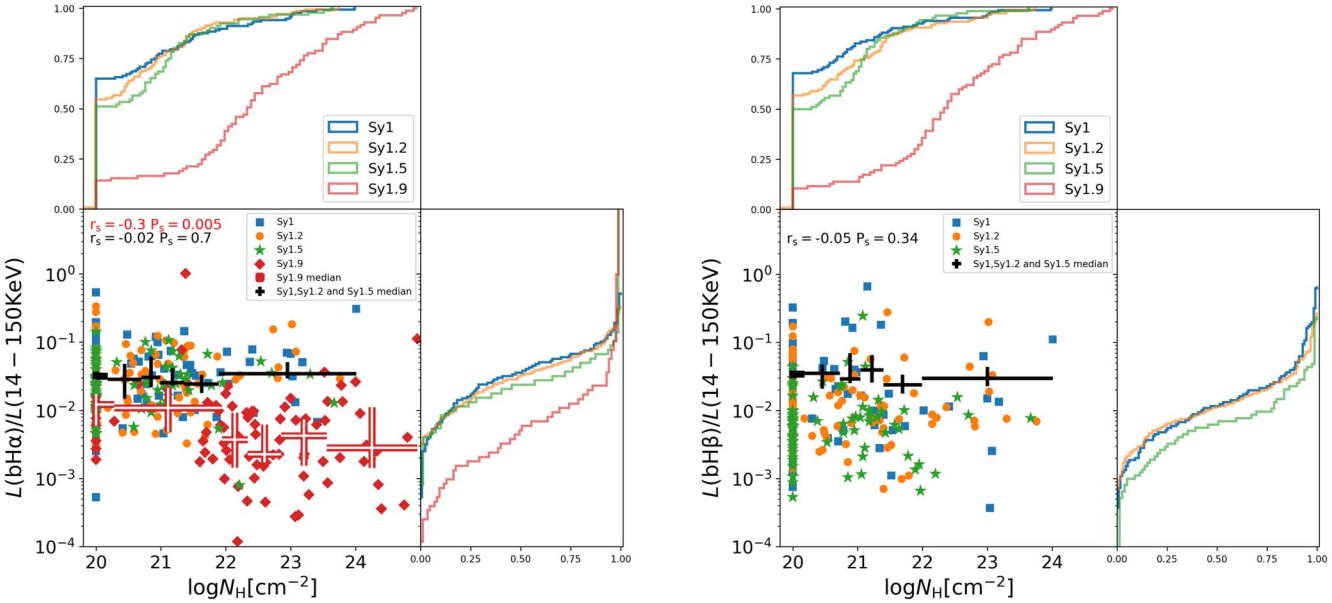

Figure 8. Broad Balmer line strength relative to ultrahard X-rays for $L(\mathrm{bH}\alpha)/L_{14-150\ \mathrm{keV}}$ (left) and $L(\mathrm{bH}\beta)/L_{14-150\ \mathrm{keV}}$ (right), vs. line-of-sight column density, N_H, and the projected distributions of these quantities. Broad-line BASS/DR2 AGNs of various AGN subclasses are marked with different colors and symbols (see legend). Large crosses represent the median values of $L(\mathrm{bH}\alpha)/L_{14-150\ \mathrm{keV}}$ and $L(\mathrm{bH}\beta)/L_{14-150\ \mathrm{keV}}$ within equally spaced bins of $\log N_\mathrm{H}$ and the corresponding 90% confidence intervals as determined from bootstrapping. Black thin crosses represent Types 1, 1.2, and 1.5 AGNs, while thick red crosses represent Type 1.9 sources. Type 1.9 AGNs typically have $L(\mathrm{bH}\alpha)/L_{14-150\ \mathrm{keV}}$ that are significantly lower than those of Types 1–1.5 AGNs, but only in the $\log(N_\mathrm{H}/\mathrm{cm}^{-2}) \gtrsim 22$ regime.

probability of having the $\log N_{\rm H}$ distribution in Sy1.9s to be drawn from the same $\log N_{\rm H}$ distribution as of Sy1–1.5s, are $\ll 10^{-10}$ (for both tests).

Second, the left panel of Figure 8 shows that the median $L(\mathrm{bH}\alpha)/L_{14-150\,\mathrm{keV}}$ ratio in Sy1–1.5 AGNs stays roughly constant across the full range in $\log N_{\rm H}$ covered by our sample. The same behavior is observed in the right panel where the median $L(\mathrm{bH}\beta)/L_{14-150\,\mathrm{keV}}$ is also roughly constant within the full $\log N_{\rm H}$ range. For Sy1.9 AGNs, however, the behavior is more complex and can be split into two different regimes, with sources having column densities either above or below roughly $\log(N_{\rm H}/\mathrm{cm}^{-2}) = 22$. In the $\log(N_{\rm H}/\mathrm{cm}^{-2}) < 22$ regime, the $L(\mathrm{bH}\alpha)/L_{14-150\,\mathrm{keV}}$ ratios of Sy1.9 sources are broadly consistent with those of Sy1–1.5 sources, with the former being only slightly lower than the latter (red versus black crosses, respectively, in the left panel of Figure 8). Specifically, for $20 < \log(N_{\rm H}/\mathrm{cm}^{-2}) < 22$ AGNs, the median $L(\mathrm{bH}\alpha)/L_{14-150\,\mathrm{keV}}$ for Sy1.9s is $(11^{+6}_{-4}) \times 10^{-3}$, compared to $(34^{+4}_{-3}) \times 10^{-3}$ for Sy1–1.5s. In the $\log(N_{\rm H}/\mathrm{cm}^{-2}) > 22$ regime, the $L(\mathrm{bH}\alpha)/L_{14-150\,\mathrm{keV}}$ ratios of Sy1.9s are significantly lower than those of Sy1–1.5s. Specifically, the corresponding median values for sources with $22 < \log(N_{\rm H}/\mathrm{cm}^{-2}) < 24$ are $(4^{+2}_{-1}) \times 10^{-3}$ and $(29^{+8}_{-7}) \times 10^{-3}$ for Sy1.9s and Sy1–1.5s, respectively. The $L(\mathrm{bH}\alpha)/L_{14-150\,\mathrm{keV}}$ ratios of Sy1.9 sources with $\log(N_{\rm H}/\mathrm{cm}^{-2}) > 22$ are thus lower by a factor of $\sim$8.5 than what is found for the Sy1–1.5 AGN population. This difference is statistically significant, as confirmed by the appropriate KS and WRS tests ($P < 10^{-6}$ for both tests). The more general trend of (monotonically) decreasing $L(\mathrm{bH}\alpha)/L_{14-150\,\mathrm{keV}}$ with increasing $N_{\rm H}$ in Sy1.9 AGNs is only marginally significant, with $P \simeq 0.03$ and 0.13 for the Spearman and Pearson correlation tests, respectively.

We conclude that for AGNs with relatively weak broad Balmer line emission, that is, Type 1.9 AGNs, the (relative) strength of the broad Hα emission line at fixed ultrahard X-ray luminosity is linked to the presence of large gas columns along the line of sight, independently determined from X-ray spectral modeling. This may suggest that in Type 1.9 AGNs, but not in Types 1–1.5s, the broad Hα emission is partially absorbed by the same gas that also accounts for the large neutral gas columns.

The association of weak broad Hα emission with dust obscuration may be challenged by the typical column densities of order $\log(N_{\rm H}/\mathrm{cm}^{-2}) \simeq 23$ in our Sy1.9s: For a standard (Galactic) dust-to-gas ratio (Bohlin et al. 1978), the corresponding optical extinction ($A[\mathrm{H}\alpha] \sim 30$ mag) would be expected to completely suppress the optical AGN broad-line emission. The fact that our Sy1.9s do show broad Hα emission therefore requires either (1) that the Balmer emission is only partially obscured or (2) that the dust-to-gas ratio of the obscurer is significantly lower than ISM values. Partial obscuration of the broad Hα line could also occur if the line of sight to the BLR "grazes" the obscuring torus, which completely obscures the line of sight to the (X-ray-emitting) central engine (see discussion in, e.g., Goodrich 1995; Trippe et al. 2010).

A drastically different interpretation is that the narrow Hα emission in our Sy1.9s is intrinsically strong compared to the broad Hα emission, as is common in low-luminosity AGNs (Stern & Laor 2012). Strong narrow-line emission may be due to galaxy-scale gas covering a large fraction of sight lines to the AGN. A large abundance of gas in the galaxy may also enhance the typical hydrogen columns along the line of sight to the X-ray source as seen in our Sy1.9s (see also, e.g., Maiolino & Rieke 1995; Koss et al. 2021). This latter scenario, however, stands in contrast to some evidence for the high-$N_{\rm H}$ material in (BASS) AGNs to be confined to the nuclear region (e.g., Ricci et al. 2017b) and in contrast to constraints on galaxy-wide contributions to $N_{\rm H}$ (e.g., $\log(N_{\rm H}/\mathrm{cm}^{-2}) \lesssim 22.5$ inferred by Buchner & Bauer 2017; see also Ramos Almeida & Ricci 2017 for a review).

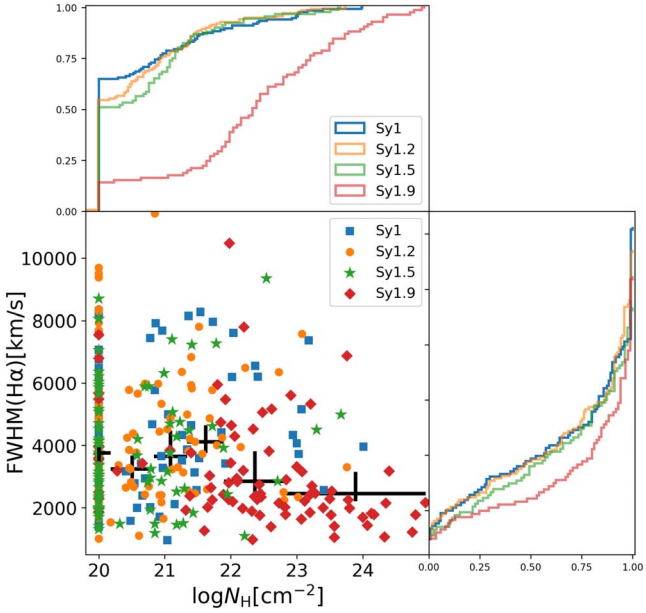

Figure 9. Hα FWHMs vs. $N_{\rm H}$ and the projected distribution of these quantities for Sy1 (light blue), Sy1.2 (orange), Sy1.5 (light green), and Sy1.9 (red) AGNs. Horizontal error bars represent the bin edges, and vertical error bars represent the errors in the median FWHM from each bin estimated from bootstrapping. For completeness, Figure 16 shows the complementary FWHM(Hβ) vs. $N_{\rm H}$ parameter space.

Because the BASS/DR2 data do not have the spatial information required to thoroughly test this alternative scenario, we next turn our attention to the kinematic information available for our BASS/DR2 AGNs, and particularly for the Sy1.9s, to gain further insight regarding the interplay between (X-ray) obscuration and (suppressed) broad Balmer emission and the nature of the gas structures at play.

4.3. Attenuation of the Highest-velocity Hα Emission Region

After establishing a link between the detailed attenuation of broad Balmer line emission and X-ray-determined line-of-sight column densities, we now use our BASS/DR2 AGN sample to better understand the nature of the relevant obscuring material.

In Figure 9 we show FWHM(Hα) versus $\log N_{\rm H}$, as well as the respective projected cumulative distributions for these quantities, for our sample of broad-line BASS/DR2 AGNs. For the sake of completeness, we also show a similar figure for FWHM(Hβ) in Figure 16 (in Appendix F). A simple visual inspection of Figure 9 suggests that sources with no detected broad Hβ emission (i.e., Sy1.9 sources) are clustered toward higher column densities ($\log(N_{\rm H}/\mathrm{cm}^{-2}) \gtrsim 22$) and narrower H$\alpha$ (FWHM(Hα) $\lesssim 3000\,\mathrm{km\,s^{-1}}$), compared with the $\log N_{\rm H}$ and FWHM(Hα) distribution of sources with detected broad Hβ (i.e., Sy1–1.5s). Indeed, formal KS and WRS statistical tests indicate that the FWHM(Hα) distribution in Sy1.9 is significantly different from that of Sy1–1.5 s ($P \lesssim 10^{-5}$ for the null hypotheses of both tests). The broad Hα emission lines in

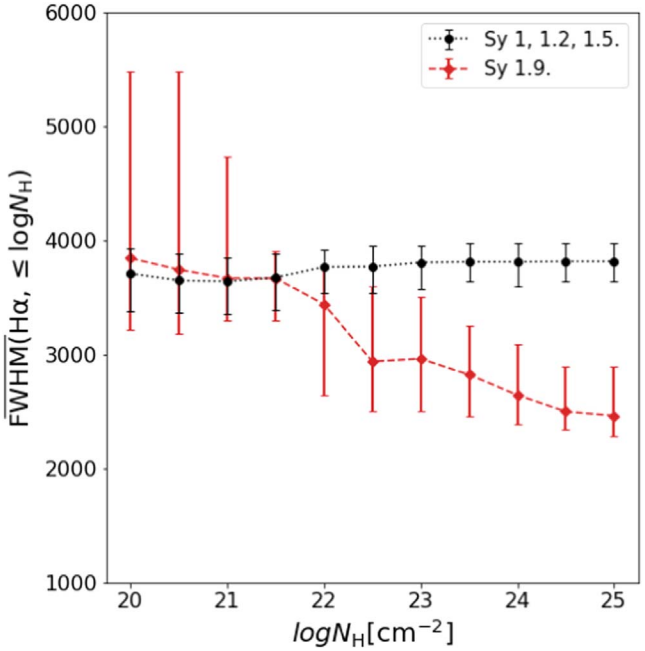

Figure 10. Median FWHM(Hα) for objects with $N_{\rm H}$ smaller than the $N_{\rm H}$ in the $\log N_{\rm H}$ (horizontal) axis. The error bars are obtained from bootstrapping and correspond to a confidence level of 90%. Type 1.9 AGNs, which tend to have higher column densities ($\log(N_{\rm H}/{\rm cm}^{-2}) > 22$) typically also have narrower Hα broad emission lines.

Sy1.9s are thus generally narrower than in Sy1–1.5s. More specifically, most Sy1.9s with $22 < \log(N_{\rm H}/{\rm cm}^{-2}) < 24$ have FWHM(Hα) $\lesssim 2500$ km s^{-1}, and the median value for such sources is 2452^{+494}_{-197} km s^{-1}, compared to a median FWHM (Hα) in Sy1–1.5s of 4337.0^{+1159}_{-610} km s^{-1} (across the entire $\log N_{\rm H}$ range). In contrast, the median FWHM(Hα) in Sy1.9s with $\log(N_{\rm H}/{\rm cm}^{-2}) < 22$ (3598^{+358}_{-316} km s^{-1}) is consistent with that of Sy1–1.5s (3677^{+142}_{-157} km s^{-1}).

To further illustrate this point, in Figure 10 we show the median FWHM(Hα) of Sy1–1.5s and Sy1.9s, which have $\log N_{\rm H}$ smaller than (or equal to) the corresponding value on the $\log N_{\rm H}$ (horizontal) axis. Evidently, for $\log(N_{\rm H}/{\rm cm}^{-2}) \lesssim 21.5$, the median values of FWHM(Hα) in Sy1–1.5s and in Sy1.9s are in good agreement. However, when $\log(N_{\rm H}/{\rm cm}^{-2}) \gtrsim 21.5$, Sy1.9s start to show narrower profiles than Sy1–1.5s, with a clear break point around $\log(N_{\rm H}/{\rm cm}^{-2}) \gtrsim 23$ where the difference becomes more prominent and exceeds the 90% confidence level (that is, exceeds the corresponding error bars).

In order to further characterize the apparent high-velocity suppression in the broad Hα profiles, in the left panel of Figure 11 we show $L({\rm bH}\alpha)/L_{14-150\,{\rm keV}}$ versus FWHM(Hα) for the Sy1–1.5 and Sy1.9 sources, with large crosses representing the median values within the FWHM(Hα) bins (and corresponding error bars; see the figure caption). Figure 11 (left) shows that, in general, Sy1.9s tend to have systematically lower $L({\rm bH}\alpha)/L_{14-150\,{\rm keV}}$ ratios across the full range of FWHM(Hα), compared to Sy1–1.5 sources. Moreover, the Sy1.9s with the narrowest Hα profiles (FWHM(Hα) $\lesssim 3000$ km s^{-1}) show yet weaker broad Hα (in terms of $L({\rm bH}\alpha)/L_{14-150\,{\rm keV}}$) than their broader-profile counterparts (i.e., Sy1.9s with $3000 \lesssim {\rm FWHM(H}\alpha)/{\rm km\,s^{-1}} \lesssim 5000$).

The right panel of Figure 11 shows $L({\rm bH}\alpha)/L_{14-150\,{\rm keV}}$ versus $\log N_{\rm H}$ for all our broad-line AGNs, irrespective of their subclass (see Figure 8, left), with each AGN color-coded by its FWHM(Hα). It is again evident that the FWHM(Hα) of heavily obscured broad-line AGNs, mostly dominated by Type 1.9 sources, show narrow and weak broad Hα emission lines. We note here that the general trend of decreasing $L({\rm bH}\alpha)/L_{14-150\,{\rm keV}}$ with increasing $\log N_{\rm H}$, among all AGNs in our sample, is highly significant ($P \simeq 10^{-7}$, as indicated).

With the insights gained from Figures 8, 9, and 11, we infer that the heavily obscured Type 1.9 AGNs ($\log(N_{\rm H}/{\rm cm}^{-2}) \gtrsim 22.5$) generally show narrower and weaker Hα broad-emission-line profiles (i.e., lower $L({\rm bH}\alpha)/L_{14-150\,{\rm keV}}$), compared with (lower-$N_{\rm H}$) Types 1–1.5 AGNs.

Combining these findings with those presented in Section 4.2, we conclude that our BASS/DR2 sample shows evidence for the attenuation of the broad Hα line emission in Type 1.9 AGNs to predominantly affect the highest-velocity line-emitting gas. Thus, the obscuring material (which is also related to the higher column densities) must be, at least partially, located on scales comparable with the innermost parts of the BLR.

In two parallel BASS studies, NIR spectroscopy is used to model (broad) Paschen emission lines (den Brok et al. 2022; Ricci et al. 2022). One of the results of the den Brok et al. (2022) study is that the FWHM ratio between the NIR and Hα lines in Sy1.9s increases monotonically (from $\sim$1.2 to 2) with increasing line-of-sight obscuration (from $\log(N_{\rm H}/{\rm cm}^{-2}) = 21$ to $\log(N_{\rm H}/{\rm cm}^{-2}) = 25$). In principle, this may further support the scenario in which the highest-velocity Hα-emitting regions tend to be suppressed by obscuration. However, this finding is based on a limited number of sources ($\sim$10). Moreover, the Ricci et al. (2022) study essentially finds n*o* statistically significant trend between the FWHM ratio and $N_{\rm H}$, at least up to $\log(N_{\rm H}/{\rm cm}^{-2}) \simeq 23$.

4.4. Comparing Broad-line-based and Stellar-velocity-based M_{BH} Estimates in AGNs

In this section we provide a preliminary analysis of the differences that we find between $M_{\rm BH}$ estimates derived from broad Hα emission lines ($M_{\rm BH,BLR}$, from this paper) and those derived from the stellar velocity dispersion ($\sigma_\star$) measured in the AGN hosts ($M_{{\rm BH},\sigma_\star}$).

The $\sigma_\star$ measurements are described in detail in a dedicated BASS/DR2 paper (Koss et al. 2022c; see also T. Caglar et al., in preparation). Here we briefly note that these $\sigma_\star$ measurements are based on high-quality spectroscopy and analysis of the spectral regions that include the Ca II H+K $\lambda\lambda$3935, 3968, Mg I λ5175, and/or calcium triplet (near 8500 Å) absorption features. The corresponding $M_{{\rm BH},\sigma_\star}$ estimates are then derived through the relation of Kormendy & Ho (2013). In principle, aperture size effects may be an important factor in $\sigma_\star$ estimates, particularly for surveys that cover a wide redshift range. In practice, however, most of our spectra were taken with slits of $\sim$1.″5 width, corresponding to $\sim$0.5–3.6 kpc scales for BASS AGNs at $z \simeq 0.015$–0.14, which encompasses 80% of our sources. Moreover, large galaxy samples show a rather limited diversity of $\sigma_\star$ radial profiles ($\lesssim$15% variation; Ziegler & Bender 1997; Cappellari et al. 2006; Falcón-Barroso et al. 2017). We therefore expect only about 15% systematic uncertainty in our $\sigma_\star$ estimates.

In the left panel of Figure 12, we directly compare the two sets of $M_{\rm BH}$ estimates—from broad Hα emission ($M_{\rm BH,BLR}$) and from $\sigma_\star$ ($M_{{\rm BH},\sigma_\star}$), for the 75 BASS/DR2 AGNs for which both types of measurements are available. $M_{{\rm BH},\sigma_\star}$ estimates are

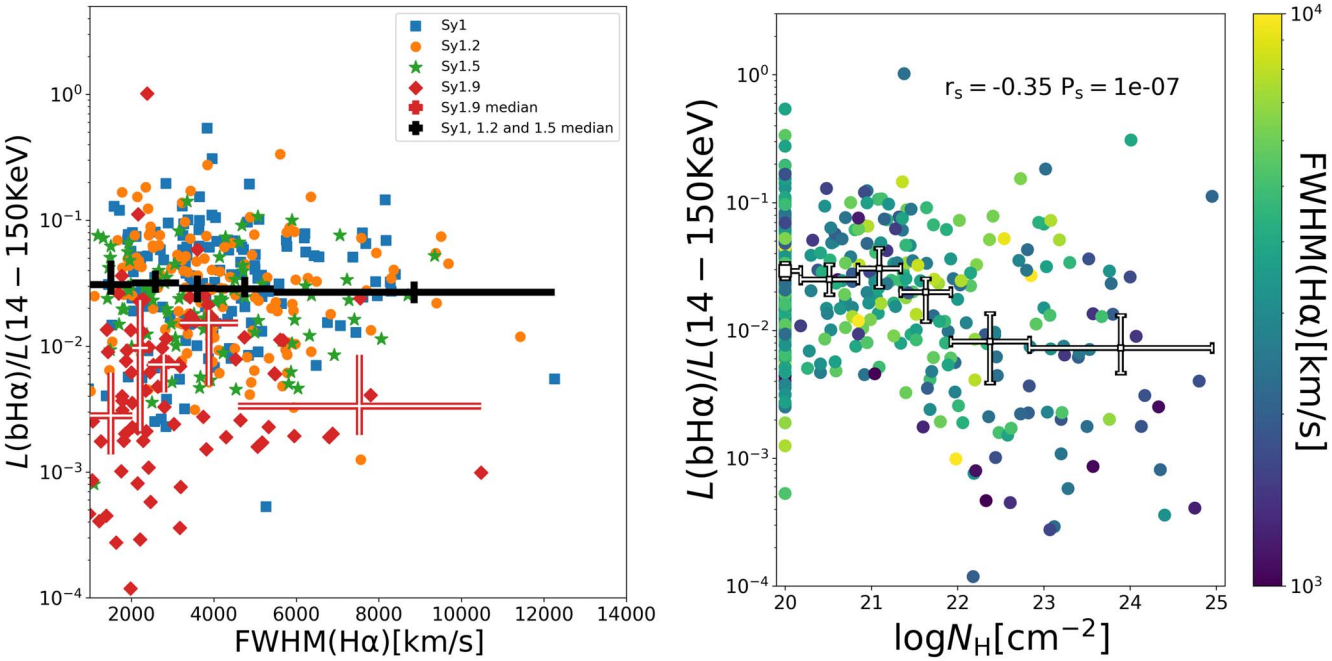

Figure 11. Left: $L(\mathrm{H}\alpha)/L(14\text{–}150$ KeV) vs. FWHM(Hα). Right: $L(\mathrm{H}\alpha)/L(14\text{–}150$ KeV) vs. $\log N_{\mathrm{H}}$ color-coded by FWHM(Hα). The vertical error bar squares represent the median values of $L(\mathrm{H}\alpha)/L(14\text{–}150$ KeV) after binning in FWHM(Hα) (left panel) and $\log N_{\mathrm{H}}$ (right panel) in equally spaced quantiles. Horizontal error bars represent the bin edges and vertical error bars the errors in the median $L(\mathrm{H}\alpha)/L(14\text{–}150$ KeV) estimated from bootstrapping.

generally larger than $M_{\mathrm{BH,BLR}}$, with median deviations of ∼0.69 and ∼0.89 dex for Sy1–1.5 and Sy1.9 sources, respectively. This result is in agreement with the recent studies of Caglar et al. (2020) on a sample of 19 local X-ray-selected AGNs from the LLAMA project (Davies et al. 2015), where they find median offsets of 0.60 and 1.0 dex for Sy1s and Sy1.9s, respectively.[38]

In the right panel of Figure 12, we present the differences between the two types of M_{BH} estimates, in terms of $\Delta \log M_{\mathrm{BH}} \equiv \log(M_{\mathrm{BH,BLR}}/M_{\mathrm{BH},\sigma_\star})$, versus line-of-sight column densities, $\log N_{\mathrm{H}}$. When considering all available data points, there is a large scatter and no clear correlation between the two quantities. However, given the difficulties in measuring $\sigma_\star$, especially in systems where the optical continuum is AGN dominated, we also consider a restricted subset of measurements, for which the uncertainties on $M_{\mathrm{BH},\sigma_\star}$ measurements are below 0.1 dex (white filled circles). For this subset of higher-quality measurements, we can see that $\Delta \log M_{\mathrm{BH}}$ is roughly −0.74 dex even for unobscured and mildly obscured AGNs, i.e., $\log(N_{\mathrm{H}}/\mathrm{cm}^{-2}) \leqslant 22.5$. This is in agreement with the findings of previous studies, such as Woo et al. (2013, 2015) and Shankar et al. (2016), and more recently by Shankar et al. (2019) and Caglar et al. (2020). These works explored several scenarios to explain this offset, which we discuss below. For higher column densities, above $\log(N_{\mathrm{H}}/\mathrm{cm}^{-2}) \approx 22$—that is, the regime dominated by Sy1.9s and where dust is expected to more strongly affect $L(\mathrm{bH}\alpha)$ measurements—$\Delta \log M_{\mathrm{BH}}$ further decreases, strongly and monotonically, from about −0.74 dex to −1.94 dex at $\log(N_{\mathrm{H}}/\mathrm{cm}^{-2}) \simeq 24$. A formal fit of our robustly measured AGNs with $\log(N_{\mathrm{H}}/\mathrm{cm}^{-2}) \geqslant 22.5$, derived using the `emcee` MCMC sampler yields the best-fit relation

$$\Delta \log M_{\mathrm{BH}} = (-0.64^{+0.26}_{-0.29}) \times \log(N_{\mathrm{H}}/10^{22}\,\mathrm{cm}^{-2}) - (0.52^{+0.20}_{-0.23}), \quad (4)$$

where the quoted uncertainties represent 95% confidence intervals. A fit using the BCES(Y|X) method provides a highly consistent relation, with slope and intercept of -0.59 ± 0.09 and 0.62 ± 0.11, respectively. The reason for this difference can be directly attributed to the fact that Sy1.9 sources show systematically lower $L(\mathrm{bH}\alpha)/L_{14-150\,\mathrm{keV}}$ and narrower FWHM(Hα) (as shown in detail in the preceding sections), which contributes to lower $M_{\mathrm{BH,BLR}}$ (see Equation (1) and Table 3).

One possible explanation for the discrepancy between broad-line-based and host-based determinations of M_{BH} in nearby AGNs, as discussed in Shankar et al. (2016, 2019), is that the M_{BH}–$\sigma_\star$ relation determined for inactive galaxies is biased against low-mass BHs because of the difficulties in resolving the sphere of influence and subsequently determine the BH mass in such systems. According to these analyses, this bias artificially flattens the power-law index and increases the intercept of the observed M_{BH}–$\sigma_\star$ relation of inactive galaxies. These, in turn, may amount to a discrepancy of about 0.7 dex with respect to the (assumed) intrinsic M_{BH}–$\sigma_\star$ relation—in broad agreement with what is seen in our analysis of the BASS/DR2 sample, as well as other AGN samples.

Two additional possible explanations are related to selection biases against low and high luminosities in the sample of reverberation-mapped, broad-line AGNs that is used to calibrate BLR-based mass prescriptions, as discussed in Woo et al. (2013). On one hand, this RM sample can be slightly biased against low-luminosity AGNs and therefore against low-mass SMBHs because of their weak broad emission lines. On the other hand, a more important bias in such a sample is

[38] The virial factor f of $M_{\mathrm{BH,BLR}}$ in Figure 12 has been rescaled to 1.14 to better match the virial factor used in Kormendy & Ho (2013), which is in turn used to estimate $M_{\mathrm{BH},\sigma_\star}$ in BASS/DR2 (Koss et al. 2022c).

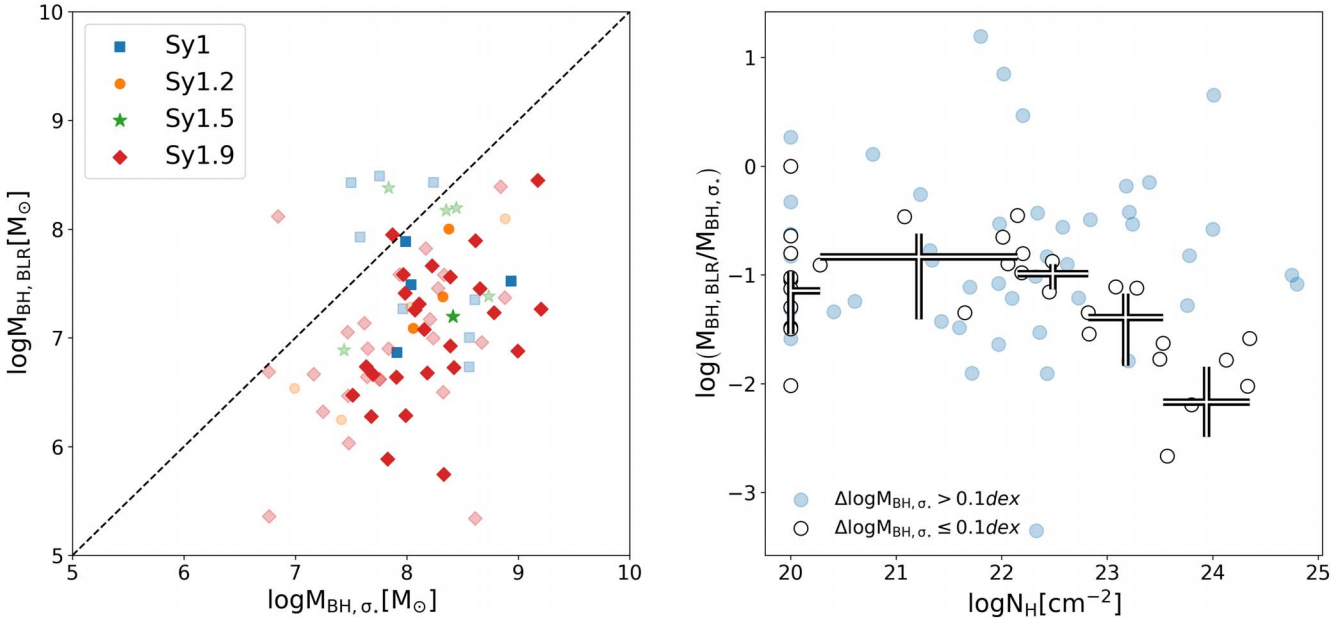

Figure 12. Left: broad-Hα-based vs. $\sigma_\star$-based $M_{\rm BH}$ estimates. Right: $\log(M_{\rm BH,BLR}/M_{\rm BH,\sigma_\star})$ vs. $\log N_{\rm H}$. In both panels, light-shaded symbols mark objects for which the measurement-related (i.e., fitting-related) uncertainties on $M_{\rm BH}$ estimates from $\sigma_\star$, $\Delta \log M_{\rm BH,\sigma_\star}$, are larger than 0.1 dex.

against luminous AGNs that are expected to preferentially harbor high-mass SMBHs. This is due to a variability bias caused by the anticorrelation between the amplitude of variability and AGN luminosity (e.g., Caplar et al. 2017 and references therein), which makes it difficult to measure the reverberation time lags in the most luminous systems. Another issue with highly luminous systems highlighted by Woo et al. (2013) is the great difficulty in measuring $\sigma_\star$ when the optical spectrum is dominated by a prominent, accretion-disk-powered component, which dilutes the weak stellar absorption features (see, e.g., Grier et al. 2013). The study by Woo et al. (2013) explicitly showed that addressing these limitations of the RM sample can indeed account for the observed discrepancies seen between BLR-based and host-based determinations of $M_{\rm BH}$.

A final possibility is that the discrepancies between broad-line-based and $\sigma_\star$-based $M_{\rm BH}$ estimates are caused by an overall different phase of evolution of the inactive and active galaxies populations. In such a scenario, the SMBHs of those galaxies observed to be active are still growing and have yet to reach their "final" location in the $M_{\rm BH}$–$\sigma_\star$ plane. While growing, active systems may indeed be located "below" the BH-host relations of inactive galaxies and will eventually reach them, as expected from some coevolutionary models (e.g., Silk & Rees 1998; King 2003) and simulations (e.g., Anglés-Alcázar et al. 2017; Bower et al. 2017; Lapiner et al. 2021). We note that the (late) evolution of active galaxies in the $M_{\rm BH}$–$\sigma_\star$ plane is far from being well understood, and radically different scenarios have been explored in numerous studies that address the (redshift-resolved) AGN and galaxy populations (e.g., Caplar et al. 2018 and references therein).

Unfortunately, the BASS/DR2 sample cannot be used to directly address these previously published scenarios as the vast majority (50 out of 75, or 66%) of the objects in our sample with both broad-line-based and $\sigma_\star$-based $M_{\rm BH}$ estimates are Sy1.9 sources, which exhibit much larger mass discrepancies (Figure 12). Taken at face value, these large discrepancies in dust-obscured Sy1.9 mass estimates (of up to 2 dex) may hint at the possibility that dust obscuration and/or circumnuclear (dusty) gas may play a role in where a given AGN appears in the $M_{\rm BH}$–$\sigma_\star$ plane. However, our analysis has demonstrated that it is much more likely that the seemingly low broad-line-based $M_{\rm BH}$ estimates of Sy1.9s are due to the diminished emission of the (high-velocity) Hα line.

In order to more directly address the issue of $M_{\rm BH}$ discrepancies, the BASS team is pursuing two complementary directions. T. Caglar et al. (in preparation) focus on a highly complete sample of Sy1 sources with both broad-line-based and $\sigma_\star$-based estimates of $M_{\rm BH}$, and little sign of obscuration ($\log(N_{\rm H}/{\rm cm}^{-2}) \lesssim 22$). As mentioned above, Ricci et al. (2022) use NIR broad-line-based $M_{\rm BH}$ estimates in Sy1.9s using, e.g., broad Paα and Paβ lines, which are far less affected by dust (compared to Hα).

The findings presented here have important implications for the determination of $M_{\rm BH}$ in individual AGNs and for the distributions of $M_{\rm BH}$ (i.e., the BHMF) in AGN samples that are based solely on the identification of broad Hα emission. In such surveys, some portion of Sy1.9 sources may not be robustly identified (and excluded), while some portion of the ones that are identified will have $M_{\rm BH}$ measurements that are significantly underestimated (by as much as 2 dex). Consequently, this would lead to $L/L_{\rm Edd}$ being overestimated (again, by up to 2 dex). To remedy this when using large samples, one may consider focusing on those sources that have a robust identification of broad Hβ emission or in which broadband (X-ray) spectral analysis suggests limited dust obscuration ($\log(N_{\rm H}/{\rm cm}^{-2}) \lesssim 22$).

Another practical remedy would be to derive empirical corrections for the key observables, and the $M_{\rm BH}$ estimates, of Type 1.9 sources. We calibrate such corrections in the next section.

4.5. Correcting Single-epoch M_{BH}(bHα) Estimates in Type 1.9 AGNs

Our analysis shows that Type 1.9 AGNs exhibit suppression of the broad Hα line emission, particularly the highest-velocity

emission, likely caused by dust obscuration. These effects become more prominent with increasing $N_{\rm H}$. Given that the determination of $M_{\rm BH}$ from BLR properties depends (almost solely) on $L(\mathrm{bH}\alpha)$ and FWHM(Hα) measurements, these effects may have a direct impact on the determination of $M_{\rm BH}$ in AGN samples, introducing a bias of underestimated $M_{\rm BH}$ in (partially) obscured AGNs.

How can one overcome this tendency to underestimate $M_{\rm BH}$ in Sy1.9 sources? Given that our BASS/DR2 AGNs sample has only 50 Sy1.9 sources with both types of $M_{\rm BH}$ estimates (BLR-based and $\sigma_\star$-based), we prefer to provide only simple, median corrections—that is, corrections that will bring the median quantities to agreement—which can be applied to Sy1.9s in various regimes of key observables. Below we provide such corrections to $L(\mathrm{bH}\alpha)$ and FWHM(Hα) in Sy1.9 sources, using $L_{14-150\,\rm keV}$ (whenever it is available). To this end, we divide the $L(\mathrm{bH}\alpha)$/$L_{14-150\,\rm keV}$–FWHM(Hα) parameter space into three regimes. We then simply identify the multiplicative corrections in $L(\mathrm{bH}\alpha)$ and FWHM(Hα) that bring the median values of these quantities in Sy1.9s to agree with the medians of the Sy1–1.5s. The uncertainties on these corrections were derived through a bootstrapping procedure and represent the central 68th percentiles (i.e., 1σ equivalent). We also report the corresponding corrections to $\log M_{\rm BH}$, which are derived by combining the corrections in $L(\mathrm{bH}\alpha)$ and FWHM(Hα), through our $M_{\rm BH}$ prescription.

The corrections for various ranges in $L(\mathrm{bH}\alpha)/L_{14-150\,\rm keV}$ and FWHM(Hα) are:

1. FWHM(Hα)$_{\rm obs} \lesssim 2400\,\mathrm{km\,s^{-1}}$ and $L(\mathrm{bH}\alpha)/L_{14-150\,\rm keV} < 10^{-2}$:
   (a) $L(\mathrm{bH}\alpha)_{\rm corr} = (21.6^{+20.2}_{-9.8}) \times L(\mathrm{bH}\alpha)_{\rm obs}$
   (b) FWHM(Hα)$_{\rm corr} = (2.05^{+0.66}_{-0.32}) \times$ FWHM(Hα)$_{\rm obs}$
   (c) $\Delta \log M_{\rm BH} \simeq 1.28^{+0.41}_{-0.30}$ dex
2. FWHM(Hα)$_{\rm obs} \gtrsim 2400\,\mathrm{km\,s^{-1}}$ and $L(\mathrm{bH}\alpha)/L_{14-150\,\rm keV} < 10^{-2}$:
   (a) $L(\mathrm{bH}\alpha)_{\rm corr} = (8.4^{+3.9}_{-2.5}) \times L(\mathrm{bH}\alpha)_{\rm obs}$
   (b) FWHM(Hα)$_{\rm corr} = (0.93^{+0.32}_{-0.22}) \times$ FWHM(Hα)$_{\rm obs}$ (consistent with no correction).
   (c) $\Delta \log M_{\rm BH} \simeq 0.53^{+0.09}_{-0.09}$ dex
3. $L(\mathrm{bH}\alpha)/L_{14-150\,\rm keV} > 10^{-2}$:
   (a) $L(\mathrm{bH}\alpha)_{\rm corr} = (1.4^{+0.3}_{-0.4}) \times L(\mathrm{bH}\alpha)_{\rm obs}$ (consistent with no correction).
   (b) FWHM(Hα)$_{\rm corr} = (0.99^{+0.12}_{-0.34}) \times$ FWHM(Hα)$_{\rm obs}$ (no correction needed).
   (c) No correction needed for $M_{\rm BH}$.

In practice, most AGN surveys lack measurements of $L_{14-150\,\rm keV}$, which would render the above corrections impractical. First, we note that the much more common, lower-energy measurements of $L_{2-10\,\rm keV}$ may be used as a proxy for $L_{14-150\,\rm keV}$. Specifically, for a photon index of $\Gamma_{\rm X} = 1.8$, the luminosities scale as $L_{2-10\,\rm keV} = 0.42 \times L_{14-150\,\rm keV}$. Second, we have also derived an additional set of corrections, where the infrared (IR) emission serves as a proxy of the (ultrahard) X-rays, motivated by many previous studies of the link between these spectral regimes in AGNs (e.g., Lutz et al. 2004; Fiore et al. 2009; Gandhi et al. 2009; Asmus et al. 2015; Stern 2015; Lansbury et al. 2017; Ichikawa et al. 2017, and references therein). Specifically for our BASS/DR2 sample, we used the IR measurements described in Ichikawa et al. (2019) and find that the flux at (rest-frame) 12 μm shows the tightest correlation with ultrahard X-ray emission ($r_{\rm s} = 0.55$, $P_{\rm s} \ll 10^{-10}$), again consistent with previous studies (Asmus et al. 2015; Ichikawa et al. 2017). We also confirmed that $L(\mathrm{bH}\alpha)/L_{12\,\mu\rm m}$ preserves the correlation with $\log N_{\rm H}$ with a similar significance (see Figure 15 in Appendix E). Below we provide median corrections to $L(\mathrm{bH}\alpha)$, FWHM(Hα), and $M_{\rm BH}$ for Sy1.9 sources whenever $L_{12\,\mu\rm m}$ is available. For this, we have repeated our analysis while dividing the Sy1.9s in our sample into three regimes in $L(\mathrm{bH}\alpha)/L_{12\,\mu\rm m}$ and FWHM(Hα). The corresponding median corrections are:

1. FWHM(Hα)$_{\rm obs} \lesssim 2400\,\mathrm{km\,s^{-1}}$ and $L(\mathrm{bH}\alpha)/L_{12\,\mu\rm m} < 7 \times 10^{-3}$:
   (a) $L(\mathrm{bH}\alpha)_{\rm corr} = (17.0^{+16.9}_{-7.6}) \times L(\mathrm{bH}\alpha)_{\rm obs}$
   (b) FWHM(Hα)$_{\rm corr} = (1.92^{+0.41}_{-0.22}) \times$ FWHM(Hα)$_{\rm obs}$
   (c) $\Delta \log M_{\rm BH} \sim 1.40^{+0.23}_{-0.37}$ dex
2. FWHM(Hα)$_{\rm obs} \gtrsim 2400\,\mathrm{km\,s^{-1}}$ and $L(\mathrm{bH}\alpha)/L_{12\,\mu\rm m} < 10^{-2}$:
   (a) $L(\mathrm{bH}\alpha)_{\rm corr} = (16.0^{+5.4}_{-5.3}) \times L(\mathrm{bH}\alpha)_{\rm obs}$
   (b) FWHM(Hα)$_{\rm corr} = (0.88^{+0.42}_{-0.18}) \times$ FWHM(Hα)$_{\rm obs}$ (consistent with no correction).
   (c) $\Delta \log M_{\rm BH} \sim 0.68^{+0.09}_{-0.10}$ dex
3. $L(\mathrm{bH}\alpha)/L_{12\,\mu\rm m} > 10^{-2}$:
   (a) $L(\mathrm{bH}\alpha)_{\rm corr} = (2.4^{+1.1}_{-0.8}) \times L(\mathrm{bH}\alpha)_{\rm obs}$
   (b) FWHM(Hα)$_{\rm corr} = (1.03^{+0.28}_{-0.25}) \times$ FWHM(Hα)$_{\rm obs}$ (no correction needed).
   (c) $\Delta \log M_{\rm BH} \sim 0.21^{+0.10}_{-0.09}$ dex

We finally note that, as part of our search for ways to improve $M_{\rm BH}$ estimates in (Sy1.9) BASS AGNs, we have also checked the possibility that FWHM(Hα) is correlated with $L([\mathrm{O\,III}])/L(\mathrm{nH}\beta)$, as found by Baron & Ménard (2019) in their (spectral stacking) analysis of the SDSS/DR7 quasar sample. This correlation is proposed as a promising method to provide $M_{\rm BH}$ estimates for narrow-line AGNs and—in the context of the present study—may thus be used to improve mass estimates in Sy1.9 sources. We do find that FWHM(Hα) and $L([\mathrm{O\,III}])/L(\mathrm{nH}\beta)$ are correlated in our BASS/DR2 sample, with the Pearson and Spearman correlation tests resulting in $P = 0.006$ and $\approx 10^{-4}$, respectively. However, these correlations are weak ($r_{\rm s} = 0.14$ and 0.19, respectively) and the scatter is huge, which prevents us from using the correlation to improve our $M_{\rm BH}$ estimates. We stress that we are not evaluating the correlation on stacked data, as was done in Baron & Ménard (2019), but rather on individual spectra in which measuring $L([\mathrm{O\,III}])/L(\mathrm{nH}\beta)$ is much more challenging. Proper stacking analysis is beyond the scope of the present study.

5. Summary and Conclusions

In this paper, we presented broad-emission-line measurements for the second data release of the BAT AGN Spectroscopic Survey (BASS/DR2), which consists of 512 AGNs selected in the ultrahard X-rays and for which high-quality fits of the Hα, Hβ, Mg II, and/or C IV emission lines are now made available. These detailed spectral measurements are used to also determine the masses ($M_{\rm BH}$) and Eddington ratios ($L/L_{\rm Edd}$) of the SMBHs that power these AGNs. The key features of this new catalog, compared to BASS/DR1, are as follows:

1. We provide broad-line measurements and derived BH masses for 689 AGNs, of which 512 are drawn from the

70 month Swift/BAT catalog (i.e., almost 60% of the 70 month sources, which constitute the main DR2 sample). In addition, we provide measurements for 177 AGNs detected in deeper BAT data.
2. At its core, lower-redshift focus, our BASS/DR2 catalog has 445 unbeamed, $z < 0.7$ AGNs drawn from the 70 month Swift/BAT catalog, with reliable determinations of $M_{\rm BH}$ from the broad Hα and/or Hβ emission lines.
3. We provide improved spectral measurements and BH determinations for >200 BASS AGNs, for which the BASS/DR2 efforts resulted in higher-quality data and/or analysis.
4. The larger fraction of sources with a wide spectral coverage allows for a more complete identification of AGN subclasses using optical line ratios.
5. BH masses are estimated using a more consistent set of prescriptions, particularly the virial factor ($f = 1$).

The BASS/DR2 broad-emission-line catalog is released as part of this paper (in machine-readable form) and is available on the BASS website.[39]

In the second part of the paper, we used the unprecedentedly large compilation of BASS/DR2 multiwavelength data to investigate the properties of "partially obscured" broad-line systems—so-called Type 1.9 AGNs (or Sy1.9s), which show broad Hα emission lines but no bluer broad (Balmer) lines. We compared these Type 1.9 sources to those AGNs with both broad Hα and Hβ emission lines, i.e., Types 1–1.5 sources. Our main findings regarding partially obscured, Type 1.9 AGNs can be summarized as follows:

1. Type 1.9 AGNs tend to exhibit high column densities, typically $\log(N_{\rm H}/{\rm cm}^{-2}) \gtrsim 22$, compared to Types 1–1.5 AGNs, which typically have $\log(N_{\rm H}/{\rm cm}^{-2}) \lesssim 22$.
2. The strength of the broad Hα emission line (relative to the X-ray continuum) decreases with increasing $N_{\rm H}$ and is particularly suppressed in Type 1.9 AGNs. This suggests that the broad-line emission is affected by dust.
3. The broad Hα suppression particularly affects the highest-velocity parts of the line profile, i.e., the innermost parts of the Hα-emitting region in the BLR.
4. These effects result in a significant underestimation of BLR-based $M_{\rm BH}$ in Type 1.9 AGNs, with a discrepancy of 0.8 dex at $\log(N_{\rm H}/{\rm cm}^{-2}) \simeq 22.5$ and up to 2 dex at $\log(N_{\rm H}/{\rm cm}^{-2}) \simeq 24$.
5. To remedy the potential $M_{\rm BH}$ discrepancies, we provide simple, empirical corrections for L(bHα) and FWHM (Hα), applicable to Type 1.9 AGNs with either (ultra-hard) X-ray or IR measurements.

As an alternative to our corrections, if near-IR spectroscopy is available, then one may consider using $M_{\rm BH}$ prescriptions that are based on broad Paschen emission lines (e.g., Ricci et al. 2017d; Kim et al. 2018), as this spectral regime is less affected by dust.

Our work provides the community with a large, highly complete compilation of reliable determinations of $M_{\rm BH}$ (and $L/L_{\rm Edd}$), while also highlighting some of the challenges associated with partially obscured sources and with AGN surveys where broad Balmer emission lines are used for $M_{\rm BH}$ determinations. As such, we hope our catalog and analysis can be useful for detailed investigations of individual AGNs and/or of SMBH demographics in the local universe, particularly when combined with the rich compilation of multiwavelength measurements available through BASS. Several complementary works, published as part of the BASS/DR2 effort, indeed pursue such investigations.

We thank the anonymous referee for their constructive comments, which helped us improve the paper. We also thank Lea Marcotulli for her assistance with identifying beamed AGN candidates, and Jonathan Stern for his insightful comments.

B.T. acknowledges support from the Israel Science Foundation (grant No. 1849/19) and from the European Research Council (ERC) under the European Union's Horizon 2020 research and innovation program (grant agreement No. 950533). M.K. acknowledges support from NASA through ADAP award NNH16CT03C. K.O. acknowledges support from the National Research Foundation of Korea (NRF-2020R1C1C1005462). C. R. acknowledges support from the Fondecyt Iniciacion grant 11190831. We also acknowledge support from ANID grants CATA-Basal AFB-170002 (F.R., F.E.B., E.T.) and FB210003 (C.R., F.E.B., E.T., R.J.A.); FONDECYT Regular 1190818 (E. T., F.E.B.), 1191124 (R.J.A.), and 1200495 (F.E.B., E.T.); FONDECYT Postdoctorado 3180506 (F.R.) and 3210157 (A.R.); Anillo ACT172033 (E.T.); and Millennium Science Initiative ICN12_009 (MAS; F.E.B.) and Millennium Nucleus NCN19_058 (TITANs; E.T.). D.A. acknowledges funding through the European Union's Horizon 2020 and Innovation program under the Marie Sklodowska-Curie grant agreement No. 793499 (DUSTDEVILS). The work of K.I. is supported by the Japan Society for the Promotion of Science (JSPS) KAKENHI (18K13584, 20H01939).

This work relies on data collected with a large variety of facilities and analyzed using several tools. We acknowledge the work that the Swift BAT team has done to make this project possible, and the teams of the various observatories that obtained the data used in this paper. Specifically, this work is based on observations collected at the European Organisation for Astronomical Research in the Southern Hemisphere under 29 ESO programmes: 60.A-9024(A), 60.A-9421(A), 062.H-0612(A), 086.B-0135(A), 089.B-0951(A), 089.B-0951(B), 090.A-0830(A), 090.D-0828(A), 091.B-0900(B), 091.C-0934(B), 092.B-0083(A), 093.A-0766(A), 095.B-0059(A), 098.A-0062, 098.A-0635(B), 099.A-0403(A), 099.A-0403(B), 099.A-0442(A), 099.B-0785(A), 0101.A-0765(A), 0101.B-0456(B), 0101.B-0739(A), 0102.A-0433(A), 0103.A-0521(A), 0103.B-0566(A), 0104.A-0353(A), 0104.B-0959(A), 0106.A-0521(A), 385.B-1035(A), and 2100.B-5018(B).

BASS/DR2 also relies on observations from seven CNTAC programs: CN2016A-80, CN2018A-104, CN2018B-83, CN2019A-70, CN2019B-77, CN2020A-90, and CN2020B-48 (PI C. Ricci); and from NOIRLab program 2012A-0463 (PI M. Trippe). Funding for SDSS-III has been provided by the Alfred P. Sloan Foundation, the Participating Institutions, the National Science Foundation, and the US Department of Energy Office of Science. The SDSS-III website is http://www.sdss3.org/. The authors wish to recognize and acknowledge the very significant cultural role and reverence that the summit of Maunakea has always had within the indigenous Hawaiian community. We are most fortunate to have the opportunity to conduct observations from this mountain.

[39] http://www.bass-survey.com

This research made use of the NASA/IPAC Extragalactic Database (NED), which is operated by the Jet Propulsion Laboratory, California Institute of Technology, under contract with the National Aeronautics and Space Administration and the SIMBAD database, operated at CDS, Strasbourg, France (Wenger et al. 2000).

Facilities: Keck:I (LRIS), Magellan:Clay, Palomar:Hale (Doublespec), NuSTAR, Swift (XRT and BAT), VLT:Kueyen (X-Shooter), VLT:Antu (FORS2), SOAR (Goodman).

Software: `AstroPy` (Astropy Collaboration et al. 2013, 2018), `Matplotlib` (Hunter 2007), `NumPy` (Harris et al. 2020).

Appendix A
Fit-quality Examples

In Figure 13 we show several examples of Hα and Hβ fits of different fit-quality classes ($f_Q = 1$, 2, and 3), as assigned during our visual inspection of the spectra and best-fit models. We recall that only sources with $f_Q < 3$ provide acceptable spectral measurements, while those with $f_Q = 3$ should be discarded from any analysis. For the most cautious analyses, we further recommend focusing on $f_Q \leqslant 2$ (i.e., omitting objects with $f_Q = 2.5$, as we did in the present study).

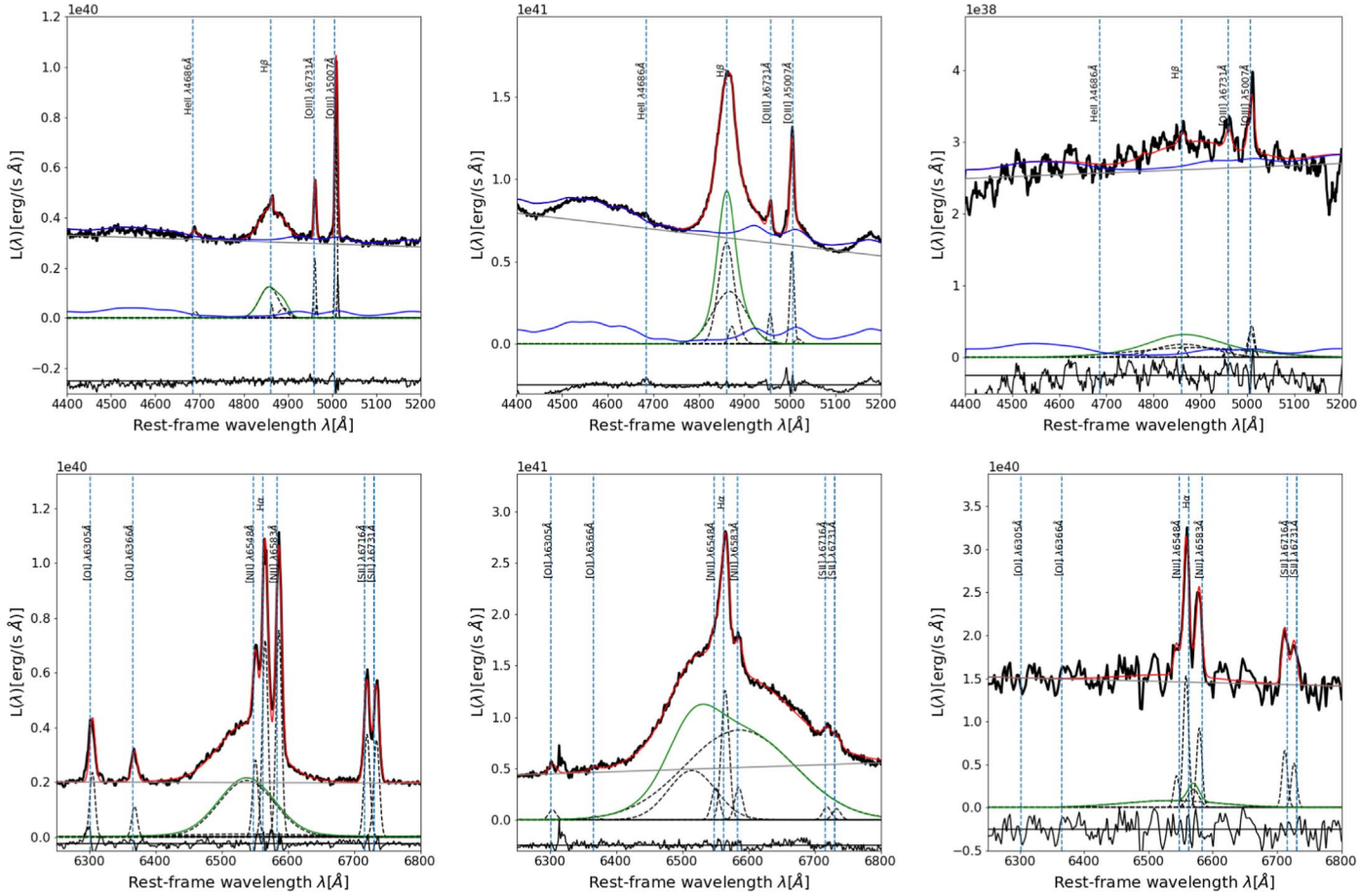

Figure 13. Spectral fit-quality flag (f_Q) examples in order of descending quality for the Hβ (top) and Hα (bottom) spectral complexes: $f_Q = 1$ (left), $f_Q = 2$ (center), and $f_Q = 3$ (right). In each case, the observed spectrum (solid black line) should be compared with the total spectral model (red). We also show the broad Balmer emission-line model (green), the blended iron emission (blue), and the narrow emission lines (dashed black). The black solid line at the bottom of each panel represents the fit residuals.

Appendix B
Comparing Broad-line Measurements in BASS DR2 and DR1

Here we compare the line-width and $M_{\rm BH}$ measurements from the new BASS/DR2 catalog presented here to those of our previous release, DR1. As mentioned in Section 2.2, compared to DR1, DR2 includes not only new optical spectra but also a more homogeneous spectral modeling procedure to derive broad-line properties and BH masses.

B.1. FWHM Comparison

In the top-left panel of Figure 14, we compare the FWHM (Hα) obtained from the BASS/DR2 catalog to those measured in DR1, for sources that were included in both catalogs. The DR2 measurements are slightly narrower than the DR1 ones, with a median offset of about 7% (see diagonal lines in Figure 14). Similarly, in the top-right panel of Figure 14, we compare the FWHM(Hβ) measurements in the DR1 and DR2 catalogs. In this case, the two sets of measurements are in very

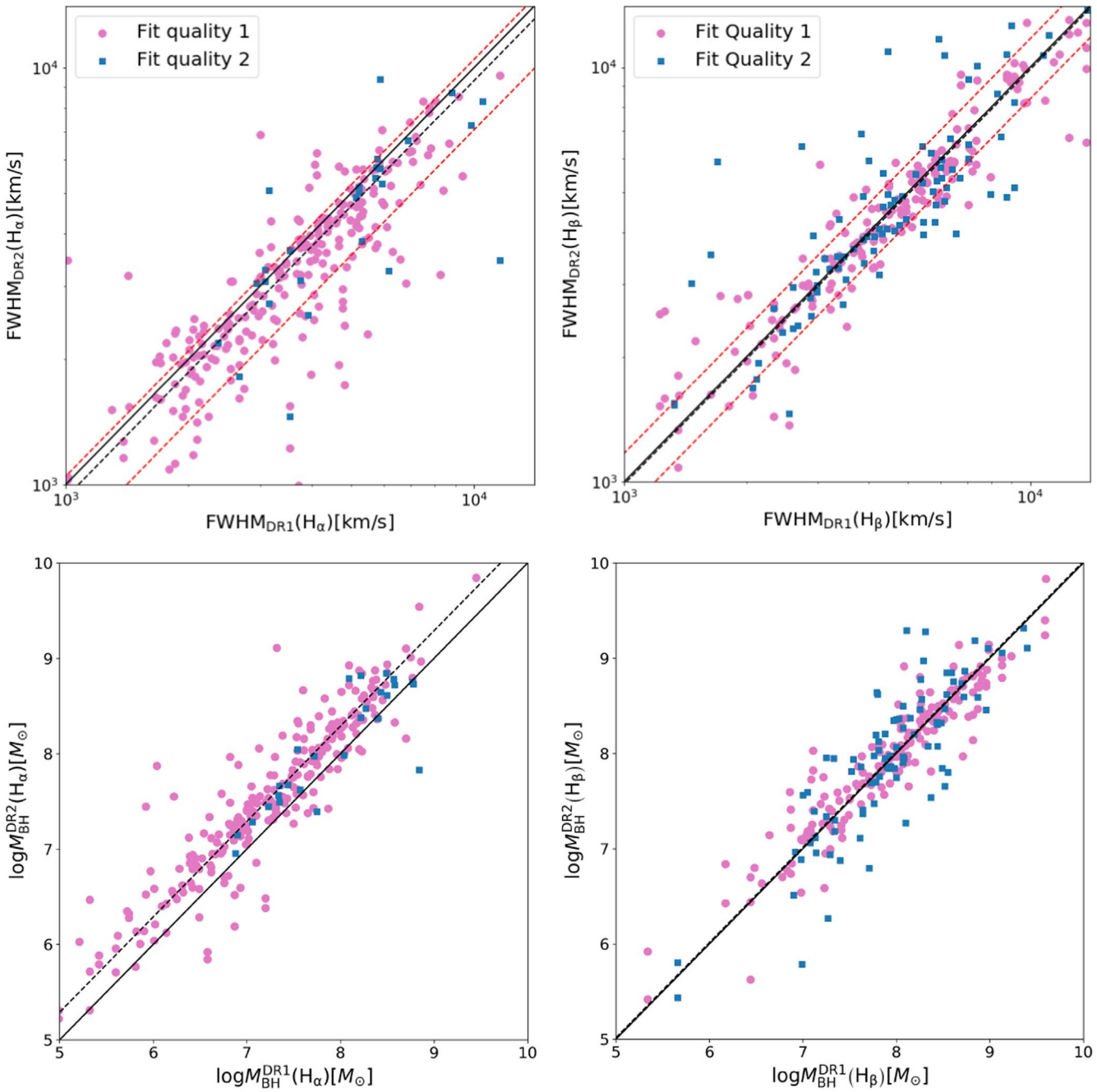

Figure 14. Comparison between DR1 and DR2 measurements: line widths (FWHM; top) and BH masses ($M_{\rm BH}$; bottom), for both Hα (left) and Hβ (right). In all panels, black solid lines represent the 1:1 relation and black dashed lines trace the median offsets between DR1 and DR2 measurements.

good agreement up to 8000 km s^{-1}, with a median offset from the 1:1 relation of only 2%. The reason for the good agreement between the DR1 and DR2 FWHM(Hβ) measurements is that in both cases we followed a very similar fitting procedure. On the other hand, the slightly larger offset in the FWHM(Hα) measurements is very likely caused by the differences in the fitting procedures—in DR1, the Hα spectral complex was modeled with rather simplistic, ad hoc procedures, while for DR2, we adopt the more elaborate and AGN-tailored procedures of Mejía-Restrepo et al. (2016).

B.2. Black Hole Mass Comparison

In the bottom panels of Figure 14 we compare the Hα-based (bottom left) and Hβ-based (bottom right) BH mass estimates obtained in DR2 to those obtained in DR1. The Hβ-based $M_{\rm BH}$ estimates from both DRs are in very good agreement, with a negligible offset (median of −0.02 dex). However, when it comes to Hα, there is a clear disagreement of 0.23 dex between DR1 and DR2 $M_{\rm BH}$ measurements, in the sense that DR2 measurements are systematically larger than DR1 ones. One of the main reasons for this discrepancy is the use of different virial factors in DR1 and DR2: While for DR1 we used $f_{\rm FWHM(H\alpha)} = 0.75$ and $f_{\rm FWHM(H\beta)} = 1$, in DR2 we instead use $f_{\rm FWHM(H\alpha)} = f_{\rm FWHM(H\beta)} = 1$. The reason for this choice is to keep consistency between the masses derived using the two emission lines and to more recent calibrations that are based on the comparison of virial (SE) and $\sigma_\star$-based $M_{\rm BH}$ estimates (e.g., Woo et al. 2015). This update of the virial factor accounts for 0.13 dex on the total offset. The remaining ∼0.1 dex is explained by the usage in DR2 of an alternative $R_{\rm BLR}$–L(bHα) calibration, which includes more RM measurements toward the low-luminosity end (Greene & Ho 2005), together with slight differences between the DR1 and DR2 FWHM(Hα) measurements.

Appendix C
Sources with Double-peaked Broad Emission Lines

Table 4 lists the BASS DR2 AGNs that we have identified to have double-peaked Hα and/or Hβ broad emission lines.

Table 4
AGNs with Double-peaked Broad Balmer Emission Lines

BAT ID	AGN Name[a]	Double-peaked...[b]	
		Hα	Hβ
45	SWIFT J0101.5–0308	0	1
48	SWIFT J0103.8–6437	1	0
107	SWIFT J0207.0+2931	1	0
135	SWIFT J0235.3–2934	1	0
136	SWIFT J0238.2–5213	1	0
147	SWIFT J0244.8+6227	0	1
170	SWIFT J0312.9+4121	1	0
172	SWIFT J0318.7+6828	1	0
207	SWIFT J0405.3–3707	1	1
270	SWIFT J0519.5–4545	1	0
371	SWIFT J0726.5+3659	1	0
372	SWIFT J0727.4-2408	1	0
403	SWIFT J0803.4+0842	1	0
413	SWIFT J0818.1+0120	1	0
414	SWIFT J0819.2–2259	0	1
454	SWIFT J0923.6–2136	1	0
525	SWIFT J1103.4+3731	1	1
607	SWIFT J1217.3+0714	1	1
618	SWIFT J1227.8–4856	0	1
686	SWIFT J1341.9+3537	0	1
690	SWIFT J1347.1+7325	1	0
713	SWIFT J1416.9-1158	1	1
715	SWIFT J1417.7+6143	1	0
776	SWIFT J1542.0–1410	1	0
800	SWIFT J1617.8+3223	1	1
876	SWIFT J1719.7+4900	1	1
882	SWIFT J1723.2+3418	1	1
907	SWIFT J1742.2+1833	1	1
923	SWIFT J1747.7–2253	1	1
1079	SWIFT J2030.2–7532	1	1
1151	SWIFT J2223.9–0207	1	1
1179	SWIFT J2301.4–5916	1	1
1196	SWIFT J2327.4+1525	1	0
1200	SWIFT J2333.9–2342	1	0

Notes.
[a] Unique AGN names from the Swift/BAT 70 month catalog.
[b] Binary flags indicating which of the two key broad Balmer lines has a double-peaked profile.

(This table is available in machine-readable form.)

Appendix D
Broad-line Measurements Catalog

Tables 5, 6, 7, and 8 describe the contents of our measurement catalogs, for the spectral regions including the broad Hα, Hβ, Mg II λ2798, and C IV λ1549 emission lines (respectively).

Table 5
Column Description for the Hα Measurements Table

Column	Name	Description
1	BAT_ID	BASS identifier
2	Subsample	The source of the optical spectrum (facility, instrument, etc.).
3	f_Q(Hα)	Quality flag for the fit: 1 for a good fit and 2 for an acceptable one
4	FWHM(bHα) [km s^{-1}]	FWHM of the broad Hα emission line.
5	Δ^- FWHM(bHα) [km s^{-1}]	Lower error on FWHM(bHα)
6	Δ^+ FWHM(bHα) [km s^{-1}]	Upper error on FWHM(bHα)
7	log L(bHα) [erg s^{-1}]	Broad Hα line luminosity
8	log L(bHα) [erg s^{-1}cm^{-2}]	Broad Hα line-integrated flux
9	Δ^- log L(bHα) [erg s^{-1}]	Lower error on log L(bHα)
10	Δ^+ log L(bHα) [erg s^{-1}]	Upper error on log L(bHα)
11	log L_{6200} [erg s^{-1}]	Monochromatic luminosity at rest-frame 6200 Å, λL_λ(6200 Å)
12	log F_{6200} [erg s^{-1}cm^{-2}]	Monochromatic flux at rest-frame 6200 Å, λF_λ(6200 Å)
13	Δ^- log L_{6200} [erg s^{-1}]	Lower error on log L_{6200}
14	Δ^+ log L_{6200} [erg s^{-1}]	Upper error on log L_{6200}
15	EW(bHα) [Å]	Rest-frame equivalent width of the broad Hα line
16	Δ^- EW(bHα) [Å]	Lower error on EW(bHα)
17	Δ^+ EW(bHα) [Å]	Upper error on EW(bHα)
18	log L_{peak}(bHα) [erg s^{-1} Å^{-1}]	Monochromatic luminosity of the broad Hα line at peak
19	log F_{peak}(bHα) [erg cm^{-2} s^{-1} Å^{-1}]	Monochromatic flux of the broad Hα line at peak
20	Δ^- log L_{peak}(bHα) [erg s^{-1} Å^{-1}]	Lower error on log L_{peak}(bHα)
21	Δ^+ log L_{peak}(bHα) [erg s^{-1} Å^{-1}]	Upper error on log L_{peak}(bHα)
22	Δv_{peak}(bHα) [km s^{-1}]	Velocity shift of the broad Hα line peak
23	$\Delta^-\Delta v_{peak}$(bHα)[km s^{-1}]	Lower error on Δv_{peak}(bHα)
24	$\Delta^+\Delta v_{peak}$(bHα) [km s^{-1}]	Upper error on Δv_{peak}(bHα)
25	Δv_{cent}(bHα) [km s^{-1}]	Velocity shift of the broad Hα line centroid
26	$\Delta^-\Delta v_{cent}$(bHα) [km s^{-1}]	Lower error on Δv_{cent}(bHα)
27	$\Delta^+\Delta v_{cent}$(bHα) [km s^{-1}]	Upper error on Δv_{cent}(bHα)
28	log M_{BH}(bHα) [$M_\odot$, GH05]	Broad Hα-based BH mass estimate, following Greene & Ho (2005)
29	Δ^- log M_{BH}(bHα) [$M_\odot$]	Lower error on log M_{BH}(bHα)
30	Δ^+ log M_{BH}(bHα) [$M_\odot$]	Lower error on log M_{BH}(bHα)
31	log L([S II]) [erg s^{-1}]	Luminosity of the narrow [S II] λ6731 emission line
32	log F([S II]) [erg s^{-1}cm^{-2}]	Integrated flux of the narrow [S II] λ6731 emission line
33	Δ log L([S II]) [erg s^{-1}]	Error on log L([S II])
34	Δv([S II]) [km s^{-1}]	Velocity shift of the [S II] λ6731 line peak/centroid
35	$\Delta\Delta v$([S II]) [km s^{-1}]	Error on Δv([S II])
36	FWHM([S II]) [km s^{-1}]	FWHM of the narrow [S II] λ6731 emission line
37	ΔFWHM([S II]) [km s^{-1}]	Error on FWHM([S II])
38	log L(nHα) [erg s^{-1}]	Luminosity of the narrow Hα line
39	log F(nHα) [erg s^{-1}cm^{-2}]	Integrated flux of the narrow Hα line
40	Δ log L(nHα) [erg s^{-1}]	Error on log L(nHα)
41	Δv(nHα) [km s^{-1}]	Velocity shift of the narrow Hα line peak/centroid
42	$\Delta\Delta v$(nHα) [km s^{-1}]	Error on Δv(nHα)
43	FWHM(nHα) [km s^{-1}]	FWHM of the narrow Hα emission line
44	ΔFWHM(nHα) [km s^{-1}]	Error on FWHM(nHα)
45	log L([N II]) [erg s^{-1}]	Luminosity of the narrow [N II] λ6584 line
46	log F([N II]) [erg s^{-1}cm^{-2}]	Integrated flux of the narrow[N II] λ6584 line
47	Δ log L([N II]) [erg s^{-1}]	Error on log L([N II])
48	Δv(nHα) [km s^{-1}]	Velocity shift of the narrow [N II] λ6584 line peak/centroid
49	$\Delta\Delta v$([N II]) [km s^{-1}]	Error on Δv([N II])
55	FWHM([N II]) [km s^{-1}]	FWHM of the narrow [N II] λ6584 emission line
51	ΔFWHM([N II]) [km s^{-1}]	Error on FWHM([N II])
52	z(DR2)	The source redshift, as reported in the BASS/DR2 catalog (Koss et al. 2022b)

Table 5
(Continued)

Column	Name	Description
53	$z_{\rm corr}$(DR2, [S II])	Updated redshift, based on NLR measurements of the [S II] emission lines from this paper
54	DR2 Type	DR2 Seyfert type according to Winkler's (1992) classification (see Section 3.1 for details).

Note. All errors are 1σ equivalent and were obtained through our spectral bootstrapping procedure. When both lower and upper errors are reported, these correspond to the 16th and 84th percentiles of the corresponding distribution. When a single error is reported, it corresponds to the standard deviation.

(This table is available in its entirety in machine-readable form.)

Table 6
Column Description for the Hβ Measurements Table

Column	Name	Description
1	BAT_ID	BASS identifier
2	Subsample	The source of the optical spectrum (facility, instrument, etc.)
3	$f_{\rm Q}$(Hβ)	Quality flag for the fit: 1 for a good fit and 2 for an acceptable one
4	FWHM(bHβ) [km s^{-1}]	FWHM of the broad Hβ emission line
5	Δ^- FWHM(bHβ) [km s^{-1}]	Lower error on FWHM(bHβ)
6	Δ^+ FWHM(bHβ) [km s^{-1}]	Upper error on FWHM(bHβ)
7	$\log L$(bHβ) [erg s^{-1}]	Broad Hβ line luminosity
8	$\log F$(bHβ) [erg s^{-1}cm^{-2}]	Broad Hβ line-integrated flux
9	$\Delta^-\log L$(bHβ) [erg s^{-1}]	Lower error on $\log L$(bHβ)
10	$\Delta^+\log L$(bHβ) [erg s^{-1}]	Upper error on $\log L$(bHβ)
11	$\log L_{5100}$ [erg s^{-1}]	Monochromatic luminosity at rest-frame 5100 Å, λL_λ(5100 Å)
12	$\log F_{5100}$ [erg s^{-1}cm^{-2}]	Monochromatic flux at rest-frame 5100 Å, λF_λ(5100 Å)
13	$\Delta^-\log L_{5100}$ [erg s^{-1}]	Lower error on $\log L_{5100}$
14	$\Delta^+\log L_{5100}$ [erg s^{-1}]	Upper error on $\log L_{5100}$
15	EW(bHβ) [Å]	Rest-frame equivalent width of the broad Hβ line
16	Δ^- EW(bHβ) [Å]	Lower error on EW(bHβ)
17	Δ^+ EW(bHβ) [Å]	Upper error on EW(bHβ)
18	$\log L_{\rm peak}$(bHβ) [erg s^{-1} Å^{-1}]	Monochromatic luminosity of the broad Hβ line at peak
19	$\log F_{\rm peak}$(bHβ) [erg cm^{-2} s^{-1} Å^{-1}]	Monochromatic flux of the broad Hβ line at peak
20	$\Delta^-\log L_{\rm peak}$(bH$\beta$) [erg s^{-1} Å^{-1}]	Lower error on $\log L_{\rm peak}$(bHβ)
21	$\Delta^+\log L_{\rm peak}$(bH$\beta$) [erg s^{-1} Å^{-1}]	Upper error on $\log L_{\rm peak}$(bHβ)
22	$\Delta v_{\rm peak}$(bHβ) [km s^{-1}]	Velocity shift of the broad Hβ line peak
23	$\Delta^-\Delta v_{\rm peak}$(bH$\beta$)[km s^{-1}]	Lower error on $\Delta v_{\rm peak}$(bHβ)
24	$\Delta^+\Delta v_{\rm peak}$(bH$\beta$) [km s^{-1}]	Upper error on $\Delta v_{\rm peak}$(bHβ)
25	$\Delta v_{\rm cent}$(bHβ) [km s^{-1}]	Velocity shift of the broad Hβ line centroid
26	$\Delta^-\Delta v_{\rm cent}$(bH$\beta$) [km s^{-1}]	Lower error on $\Delta v_{\rm cent}$(bHβ)
27	$\Delta^+\Delta v_{\rm cent}$(bH$\beta$) [km s^{-1}]	Upper error on $\Delta v_{\rm cent}$(bHβ)
28	$\log M_{\rm BH}$(bHβ) [$M_\odot$, TN12]	Broad Hβ-based BH mass estimate, following Trakhtenbrot & Netzer (2012)
29	$\Delta^-\log M_{\rm BH}$(bHβ) [$M_\odot$]	Lower error on $\log M_{\rm BH}$(bHβ)
30	$\Delta^+\log M_{\rm BH}$(bHβ) [$M_\odot$]	Lower error on $\log M_{\rm BH}$(bHβ)
31	$\log L$([O III]) [erg s^{-1}]	Luminosity of the narrow [O III] λ5007 emission line
32	$\log F$([O III]) [erg s^{-1}cm^{-2}]	Integrated flux of the narrow [O III] λ5007 emission line
33	$\Delta\log L$([O III]) [erg s^{-1}]	Error on $\log L$([O III])
34	Δv([O III]) [km s^{-1}]	Velocity shift of the [O III] λ5007 line peak/centroid
35	$\Delta\Delta v$([O III]) [km s^{-1}]	Error on Δv([O III])
36	FWHM([O III]) [km s^{-1}]	FWHM of the narrow [O III] λ5007 emission line
37	ΔFWHM([O III]) [km s^{-1}]	Error on FWHM([O III])
38	$\log L$(nHβ) [erg s^{-1}]	Luminosity of the narrow Hβ line
39	$\log F$(nHβ) [erg s^{-1}cm^{-2}]	Integrated flux of the narrow Hβ line
40	$\Delta\log L$(nHβ) [erg s^{-1}]	Error on $\log L$(nHβ)
41	Δv(nHβ) [km s^{-1}]	Velocity shift of the narrow Hβ line peak/centroid
42	$\Delta\Delta v$(nHβ) [km s^{-1}]	Error on Δv(nHβ)
43	FWHM(nHβ) [km s^{-1}]	FWHM of the narrow Hβ emission line
44	ΔFWHM(nHβ) [km s^{-1}]	Error on FWHM(nHβ)
45	z(DR2)	The source redshift, as reported in the BASS/DR2 catalog (Koss et al. 2022b)
46	$z_{\rm corr}$(DR2, [O III])	Updated redshift, based on NLR measurements of the [O III] emission lines from this paper
47	DR2 Type	DR2 Seyfert type according to Winkler's (1992) classification (see Section 3.1 for details)

Note. All errors are 1σ equivalent and were obtained through our spectral bootstrapping procedure. When both lower and upper errors are reported, these correspond to the 16th and 84th percentiles of the corresponding distribution. When a single error is reported, it corresponds to the standard deviation.

(This table is available in its entirety in machine-readable form.)

Table 7
Column Description for the Mg II λ2798 Measurements Table

Column	Name	Description
1	BAT_ID	BASS identifier
2	Subsample	The source of the optical spectrum (facility, instrument, etc.)
3	f_Q(Mg II)	Quality flag for the fit: 1 for a good fit and 2 for an acceptable one
4	FWHM(Mg II) [km s^{-1}]	FWHM of the broad Mg II emission line
5	Δ^- FWHM(Mg II) [km s^{-1}]	Lower error on FWHM(Mg II)
6	Δ^+ FWHM(Mg II) [km s^{-1}]	Upper error on FWHM(Mg II)
7	$\log L$(Mg II) [erg s^{-1}]	Broad Mg II line luminosity
8	$\log F$(Mg II) [erg s^{-1}cm^{-2}]	Broad Mg II line-integrated flux
9	$\Delta^-\log L$(Mg II) [erg s^{-1}]	Lower error on $\log L$(Mg II)
10	$\Delta^+\log L$(Mg II) [erg s^{-1}]	Upper error on $\log L$(Mg II)
11	$\log L_{3000}$ [erg s^{-1}]	Monochromatic luminosity at rest-frame 3000 Å, λL_λ(3000 Å)
12	$\log F_{3000}$ [erg s^{-1}cm^{-2}]	Monochromatic flux at rest-frame 3000 Å, λF_λ(3000 Å)
12	$\Delta^-\log L_{3000}$ [erg s^{-1}]	Lower error on $\log L_{3000}$
13	$\Delta^+\log L_{3000}$ [erg s^{-1}]	Upper error on $\log L_{3000}$
14	EW(Mg II) [Å]	Rest-frame equivalent width of the broad Mg II line
15	Δ^- EW(Mg II) [Å]	Lower error on EW(Mg II)
16	Δ^+ EW(Mg II) [Å]	Upper error on EW(Mg II)
17	$\log L_{\rm peak}$(Mg II) [erg s^{-1} Å^{-1}]	Monochromatic luminosity of the broad Mg II line at peak
18	$\log F_{\rm peak}$(Mg II) [erg s^{-1} Å^{-1}]	Monochromatic flux of the broad Mg II line at peak
19	$\Delta^-\log L_{\rm peak}$(Mg II) [erg cm^{-2} s^{-1} Å^{-1}]	Lower error on $\log L_{\rm peak}$(Mg II)
20	$\Delta^+\log L_{\rm peak}$(Mg II) [erg s^{-1} Å^{-1}]	Upper error on $\log L_{\rm peak}$(Mg II)
21	$\Delta v_{\rm peak}$(bHβ) [km s^{-1}]	Velocity shift of the broad Mg II line peak
22	$\Delta^-\Delta v_{\rm peak}$(Mg II) [km s^{-1}]	Lower error on $\Delta v_{\rm peak}$(Mg II)
23	$\Delta^+\Delta v_{\rm peak}$(Mg II) [km s^{-1}]	Upper error on $\Delta v_{\rm peak}$(Mg II)
24	$\Delta v_{\rm cent}$(Mg II) [km s^{-1}]	Velocity shift of the broad Mg II line centroid
25	$\Delta^-\Delta v_{\rm cent}$(Mg II) [km s^{-1}]	Lower error on $\Delta v_{\rm cent}$(Mg II)
26	$\Delta^+\Delta v_{\rm cent}$(Mg II) [km s^{-1}]	Upper error on $\Delta v_{\rm cent}$(Mg II)
28	$\log M_{\rm BH}$(Mg II) [$M_\odot$, MR16]	Broad Mg II-based BH mass estimate, following Mejía-Restrepo et al. (2016)
29	$\Delta^-\log M_{\rm BH}$(Mg II) [$M_\odot$]	Lower error on $\log M_{\rm BH}$(Mg II)
30	$\Delta^+\log M_{\rm BH}$(Mg II) [$M_\odot$]	Lower error on $\log M_{\rm BH}$(Mg II)
31	z(DR2)	The source redshift, as reported in the BASS/DR2 catalog (Koss et al. 2022b)
32	$z_{\rm corr}$(DR2, Mg II)	Updated redshift, based on BLR measurements of the Mg II emission line from this paper

Note. All errors are 1σ equivalent and were obtained through our spectral bootstrapping procedure. When both lower and upper errors are reported, these correspond to the 16th and 84th percentiles of the corresponding distribution. When a single error is reported, it corresponds to the standard deviation.

(This table is available in its entirety in machine-readable form.)

Table 8
Column Description for the C IV λ1549 Measurements Table

Column	Name	Description
1	BAT_ID	BASS identifier
2	Subsample	The source of the optical spectrum (facility, instrument, etc.).
3	$f_{\rm Q}$(C IV)	Quality flag for the fit: 1 for a good fit and 2 for an acceptable one
4	FWHM(C IV) [km s^{-1}]	FWHM of the broad C IV emission line
5	Δ^- FWHM(C IV) [km s^{-1}]	Lower error on FWHM(C IV)
6	Δ^+ FWHM(C IV) [km s^{-1}]	Upper error on FWHM(C IV)
7	$\log L$(C IV) [erg s^{-1}]	Broad C IV line luminosity
8	$\log F$(C IV) [erg s^{-1}cm^{-2}]	Broad C IV line-integrated flux
9	$\Delta^-\log L$(C IV) [erg s^{-1}]	Lower error on $\log L$(C IV)
10	$\Delta^+\log L$(C IV) [erg s^{-1}]	Upper error on $\log L$(C IV)
11	$\log L_{1450}$ [erg s^{-1}]	Monochromatic luminosity at rest-frame 1450 Å, λL_λ(1450 Å)
12	$\log F_{1450}$ [erg s^{-1}cm^{-2}]	Monochromatic flux at rest-frame 1450 Å, λL_λ(1450 Å)
13	$\Delta^-\log L_{1450}$ [erg s^{-1}]	Lower error on $\log L_{1450}$
14	$\Delta^+\log L_{1450}$ [erg s^{-1}]	Upper error on $\log L_{1450}$
15	EW(C IV) [Å]	Rest-frame equivalent width of the broad C IV line
16	Δ^- EW(C IV) [Å]	Lower error on EW(C IV)
17	Δ^+ EW(C IV) [Å]	Upper error on EW(C IV)
18	$\log L_{\rm peak}$(C IV) [erg s^{-1} Å^{-1}]	Monochromatic luminosity of the broad C IV line at peak
19	$\log F_{\rm peak}$(C IV) [erg cm^{-2} s^{-1} Å^{-1}]	Monochromatic flux of the broad C IV line at peak
20	$\Delta^-\log L_{\rm peak}$(C IV) [erg s^{-1} Å^{-1}]	Lower error on $\log L_{\rm peak}$(C IV)
21	$\Delta^+\log L_{\rm peak}$(C IV) [erg s^{-1} Å^{-1}]	Upper error on $\log L_{\rm peak}$(C IV)
22	$\Delta v_{\rm peak}$(bHβ) [km s^{-1}]	Velocity shift of the broad C IV line peak
23	$\Delta^-\Delta v_{\rm peak}$(C IV) [km s^{-1}]	Lower error on $\Delta v_{\rm peak}$(C IV)
24	$\Delta^+\Delta v_{\rm peak}$(C IV) [km s^{-1}]	Upper error on $\Delta v_{\rm peak}$(C IV)
25	$\Delta v_{\rm cent}$(C IV) [km s^{-1}]	Velocity shift of the broad C IV line centroid
26	$\Delta^-\Delta v_{\rm cent}$(C IV) [km s^{-1}]	Lower error on $\Delta v_{\rm cent}$(C IV)
27	$\Delta^+\Delta v_{\rm cent}$(C IV) [km s^{-1}]	Upper error on $\Delta v_{\rm cent}$(C IV)
28	$\log M_{\rm BH}$(C IV) [$M_\odot$, MR16]	Broad C IV-based BH mass estimate, following Mejía-Restrepo et al. (2016)
29	$\Delta^-\log M_{\rm BH}$(C IV) [$M_\odot$]	Lower error on $\log M_{\rm BH}$(C IV)
30	$\Delta^+\log M_{\rm BH}$(C IV) [$M_\odot$]	Lower error on $\log M_{\rm BH}$(C IV)
31	z(ref)	The source redshift, as reported in the BASS/DR2 catalog (Koss et al. 2022b)
32	$z_{\rm corr}$(DR2, C IV)	Updated redshift, based on BLR measurements of the C IV emission line from this paper

Note. All errors are 1σ equivalent and were obtained through our spectral bootstrapping procedure. When both lower and upper errors are reported, these correspond to the 16th and 84th percentiles of the corresponding distribution. When a single error is reported, it corresponds to the standard deviation.

(This table is available in its entirety in machine-readable form.)

Appendix E
Broad Hα versus Mid-IR Emission

Figure 15 shows the broad Hα to mid-IR ratios for our sample, $L(\mathrm{bH}\alpha)/L_{12\,\mu\mathrm{m}}$, versus FWHM(Hα) and $\log N_{\mathrm{H}}$. These serve to demonstrate that the mid-IR emission can substitute the ultrahard X-ray emission when deriving (or using) the corrections presented in Section 4.5.

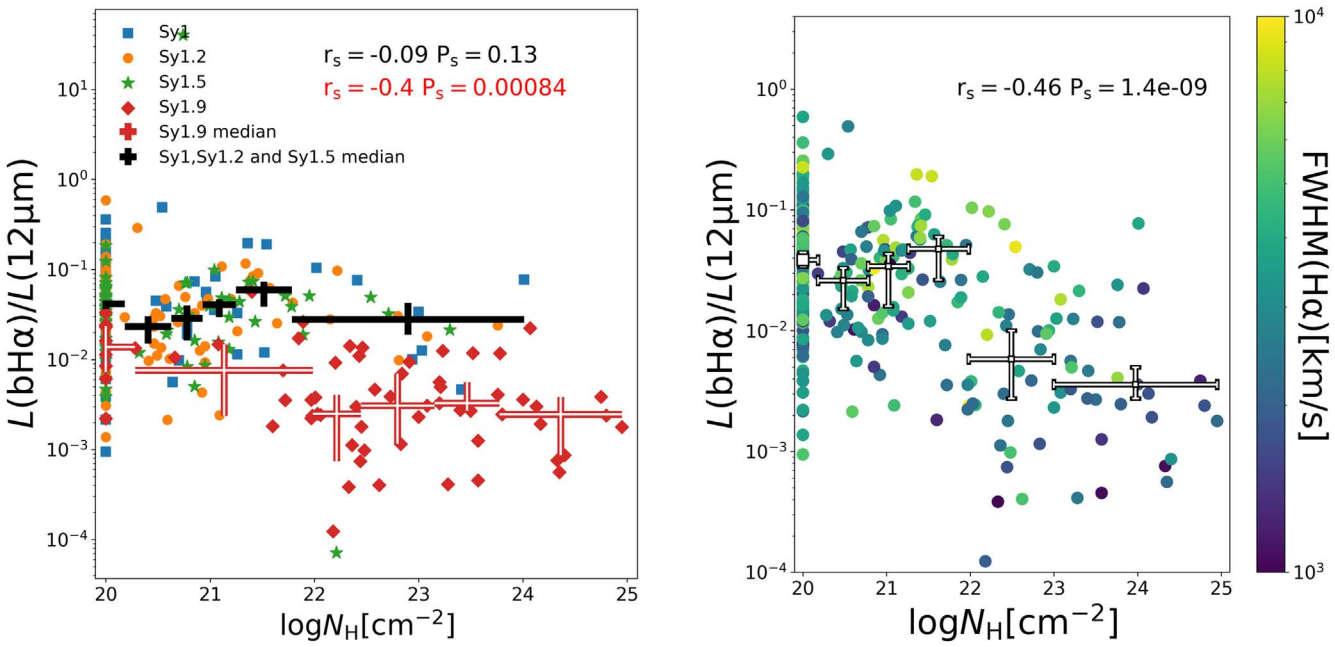

Figure 15. Left: $L(\mathrm{bH}\alpha)/L_{12\,\mu\mathrm{m}}$ vs. FWHM(Hα). Right: $L(\mathrm{bH}\alpha)/L_{12\,\mu\mathrm{m}}$ vs. $\log N_{\mathrm{H}}$ color coded by FWHM(Hα). Large crosses represent the median values of $L(\mathrm{bH}\alpha)/L_{12\,\mu\mathrm{m}}$ after binning in FWHM(Hα) (left panel) and $\log N_{\mathrm{H}}$ (right panel) in equally spaced quantiles. Horizontal error bars represent the bin edges and vertical error bars the errors in the median $L(\mathrm{bH}\alpha)/L_{12\,\mu\mathrm{m}}$ estimated from bootstrapping.

Appendix F
The Broad Hβ Line versus Column Densities

In Figure 16 we show the width of the broad Hβ emission line, FWHM(Hβ), versus the line-of-sight column density, N_H. This figure complements Figure 9.

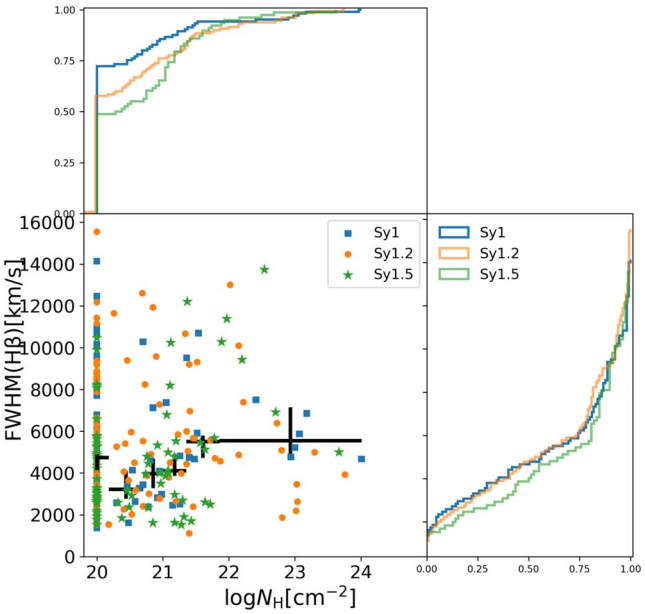

Figure 16. Hβ FWHMs vs. N_H and the projected distribution of these quantities for Sy1 (light blue), Sy1.2 (orange), Sy1.5 (light green), and Sy1.9 (red). Horizontal error bars represent the bin edges and vertical error bars represent the errors in the median FWHM from each bin estimated from bootstrapping. This figure complements Figure 9; however, in contrast to FWHM(Hα), here the median FWHM(Hβ) does not vary with $\log N_H$ (within the error bars).

ORCID iDs

Julian E. Mejía-Restrepo https://orcid.org/0000-0001-8450-7463
Benny Trakhtenbrot https://orcid.org/0000-0002-3683-7297
Michael J. Koss https://orcid.org/0000-0002-7998-9581
Kyuseok Oh https://orcid.org/0000-0002-5037-951X
Jakob den Brok https://orcid.org/0000-0002-8760-6157
Daniel Stern https://orcid.org/0000-0003-2686-9241
Meredith C. Powell https://orcid.org/0000-0003-2284-8603
Federica Ricci https://orcid.org/0000-0001-5742-5980
Turgay Caglar https://orcid.org/0000-0002-9144-2255
Claudio Ricci https://orcid.org/0000-0001-5231-2645
Franz E. Bauer https://orcid.org/0000-0002-8686-8737
Ezequiel Treister https://orcid.org/0000-0001-7568-6412
C. M. Urry https://orcid.org/0000-0002-0745-9792
Tonima Tasnim Ananna https://orcid.org/0000-0001-8211-3807
Daniel Asmus https://orcid.org/0000-0003-0220-2063
Roberto J. Assef https://orcid.org/0000-0002-9508-3667
Rudolf E. Bär https://orcid.org/0000-0001-5481-8607
Patricia S. Bessiere https://orcid.org/0000-0002-0205-5940
Leonard Burtscher https://orcid.org/0000-0003-1014-043X
Kohei Ichikawa https://orcid.org/0000-0002-4377-903X
Darshan Kakkad https://orcid.org/0000-0002-2603-2639
Nikita Kamraj https://orcid.org/0000-0002-3233-2451
Richard Mushotzky https://orcid.org/0000-0002-7962-5446
George C. Privon https://orcid.org/0000-0003-3474-1125
Alejandra F. Rojas https://orcid.org/0000-0003-0006-8681
Eleonora Sani https://orcid.org/0000-0002-3140-4070
Kevin Schawinski https://orcid.org/0000-0001-5464-0888
Sylvain Veilleux https://orcid.org/0000-0002-3158-6820

References

Ahumada, R., Prieto, C. A., Almeida, A., et al. 2020, ApJS, 249, 3
Akritas, M. G., & Bershady, M. A. 1996, ApJ, 470, 706
Ananna, T. T., Weigel, A. K., Trakhtenbrot, B., et al. 2022, ApJS, 261, 9
Anglés-Alcázar, D., Faucher-Giguère, C.-A., Quataert, E., et al. 2017, MNRAS, 472, L109
Asmus, D., Gandhi, P., Hönig, S. F., Smette, A., & Duschl, W. J. 2015, MNRAS, 454, 766
Astropy Collaboration, Robitaille, T. P., Tollerud, E. J., et al. 2013, A&A, 558, A33
Astropy Collaboration, Price-Whelan, A. M., Sipőcz, B. M., et al. 2018, AJ, 156, 123
Bär, R. E., Trakhtenbrot, B., Oh, K., et al. 2019, MNRAS, 489, 3073
Baron, D., & Ménard, B. 2019, MNRAS, 487, 3404
Baron, D., Stern, J., Poznanski, D., & Netzer, H. 2016, ApJ, 832, 8
Batiste, M., Bentz, M. C., Raimundo, S. I., Vestergaard, M., & Onken, C. A. 2017, ApJL, 838, L10
Baumgartner, W. H., Tueller, J., Markwardt, C. B., et al. 2013, ApJS, 207, 19
Bentz, M. C., Denney, K. D., Grier, C. J., et al. 2013, ApJ, 767, 149
Bentz, M. C., & Katz, S. 2015, PASP, 127, 67
Bentz, M. C., Peterson, B. M., Netzer, H., Pogge, R. W., & Vestergaard, M. 2009, ApJ, 697, 160
Bohlin, R. C., Savage, B. D., & Drake, J. F. 1978, ApJ, 224, 132
Bongiorno, A., Maiolino, R., Brusa, M., et al. 2014, MNRAS, 443, 2077
Bower, R. G., Schaye, J., Frenk, C. S., et al. 2017, MNRAS, 465, 32
Buchner, J., & Bauer, F. E. 2017, MNRAS, 465, 4348
Burtscher, L., Davies, R. I., Graciá-Carpio, J., et al. 2016, A&A, 586, A28
Cackett, E. M., Gültekin, K., Bentz, M. C., et al. 2015, ApJ, 810, 86
Caglar, T., Burtscher, L., Brandl, B., et al. 2020, A&A, 634, A114
Caplar, N., Lilly, S. J., & Trakhtenbrot, B. 2017, ApJ, 834, 111
Caplar, N., Lilly, S. J., & Trakhtenbrot, B. 2018, ApJ, 867, 148
Cappellari, M., Bacon, R., Bureau, M., et al. 2006, MNRAS, 366, 1126
Cardelli, J. A., Clayton, G. C., & Mathis, J. S. 1989, ApJ, 345, 245
Clemens, J. C., Crain, J. A., & Anderson, R. 2004, Proc. SPIE, 5492, 331
Coatman, L., Hewett, P. C., Banerji, M., et al. 2017, MNRAS, 465, 2120
Coatman, L., Hewett, P. C., Banerji, M., & Richards, G. T. 2016, MNRAS, 461, 647
Collin, S., Kawaguchi, T., Peterson, B. M., & Vestergaard, M. 2006, A&A, 456, 75
Davies, R. I., Burtscher, L., Rosario, D., et al. 2015, ApJ, 806, 127
Decarli, R., Falomo, R., Treves, A., et al. 2010, MNRAS, 402, 2453
den Brok, J. S., Koss, M. J., Trakhtenbrot, B., et al. 2022, ApJS, 261, 7
Dong, X., Wang, T., Wang, J., et al. 2008, MNRAS, 383, 581
Duras, F., Bongiorno, A., Ricci, F., et al. 2020, A&A, 636, A73
Eracleous, M., & Halpern, J. P. 1994, ApJS, 90, 1
Fabian, A. C., Vasudevan, R. V., Mushotzky, R. F., Winter, L. M., & Reynolds, C. S. 2009, MNRAS, 394, L89
Falcón-Barroso, J., Lyubenova, M., van de Ven, G., et al. 2017, A&A, 597, A48
Ferrarese, L., & Merritt, D. 2000, ApJL, 539, L9
Fiore, F., Puccetti, S., Brusa, M., et al. 2009, ApJ, 693, 447
Foreman-Mackey, D., Hogg, D. W., Lang, D., & Goodman, J. 2013, PASP, 125, 306
Gandhi, P., Horst, H., Smette, A., et al. 2009, A&A, 502, 457
Gaskell, C. M., & Harrington, P. Z. 2018, MNRAS, 478, 1660
Ginsburg, A., & Mirocha, J. 2011, PySpecKit: Python Spectroscopic Toolkit, Astrophysics Source Code Library, ascl:1109.001
Goad, M. R., Koratkar, A. P., Axon, D. J., Korista, K. T., & O'Brien, P. T. 1999, ApJL, 512, L95
Goad, M. R., Korista, K. T., De Rosa, G., et al. 2016, ApJ, 824, 11
Goodrich, R. W. 1989, ApJ, 340, 190
Goodrich, R. W. 1990, ApJ, 355, 88
Goodrich, R. W. 1995, ApJ, 440, 141
Graham, A. W. 2016, in Galactic Bulges, ed. E. Laurikainen, R. Peletier, & D. Gadotti (Cham: Springer), 263
Greene, J. E., & Ho, L. C. 2005, ApJ, 630, 122

Greene, J. E., & Ho, L. C. 2007, ApJ, 667, 131
Grier, C. J., Peterson, B. M., Horne, K., et al. 2013, ApJ, 764, 47
Grupe, D., Beuermann, K., Mannheim, K., & Thomas, H. C. 1999, A&A, 350, 805
Grupe, D., Beuermann, K., Thomas, H. C., Mannheim, K., & Fink, H. H. 1998, A&A, 330, 25
Harris, C. R., Millman, K. J., van der Walt, S. J., et al. 2020, Natur, 585, 357
Hunter, J. D. 2007, CSE, 9, 90
Ichikawa, K., Ricci, C., Ueda, Y., et al. 2017, ApJ, 835, 74
Ichikawa, K., Ricci, C., Ueda, Y., et al. 2019, ApJ, 870, 31
Ishibashi, W., Fabian, A. C., Ricci, C., & Celotti, A. 2018, MNRAS, 479, 3335
Jaffarian, G. W., & Gaskell, C. M. 2020, MNRAS, 493, 930
Jahnke, K., Bongiorno, A., Brusa, M., et al. 2009, ApJL, 706, L215
Jones, D. H., Read, M. A., Saunders, W., et al. 2009, MNRAS, 399, 683
Jovanović, P., Popović, L. Č., Stalevski, M., & Shapovalova, A. I. 2010, ApJ, 718, 168
Kaspi, S., Maoz, D., Netzer, H., et al. 2005, ApJ, 629, 61
Kaspi, S., Smith, P. S., Netzer, H., et al. 2000, ApJ, 533, 631
Kelly, B. C., & Shen, Y. 2013, ApJ, 764, 45
Kim, D., Im, M., Canalizo, G., et al. 2018, ApJS, 238, 37
King, A. 2003, ApJL, 596, L27
Kormendy, J., & Ho, L. C. 2013, ARA&A, 51, 511
Koss, M., Trakhtenbrot, B., Ricci, C., et al. 2017, ApJ, 850, 74
Koss, M. J., Strittmatter, B., Lamperti, I., et al. 2021, ApJS, 252, 29
Koss, M. J., Ricci, C., Trakhtenbrot, B., et al. 2022b, ApJS, 261, 2
Koss, M. J., Trakhtenbrot, B, Ricci, C., et al. 2022a, ApJS, 261, 1
Koss, M. J., Trakhtenbrot, B, Ricci, C., et al. 2022c, ApJS, 261, 6
Popović, L. Č., Kovačević-Dojčinović, J., & Marčeta-Mandić, S. 2019, MNRAS, 484, 3180
Kozłowski, S. 2017, ApJS, 228, 9
Lamperti, I., Koss, M., Trakhtenbrot, B., et al. 2017, MNRAS, 467, 540
Lansbury, G. B., Alexander, D. M., Aird, J., et al. 2017, ApJ, 846, 20
Lapiner, S., Dekel, A., & Dubois, Y. 2021, MNRAS, 505, 172
Lawrence, A. 1991, MNRAS, 252, 586
Lutz, D., Maiolino, R., Spoon, H. W. W., & Moorwood, A. F. M. 2004, A&A, 418, 465
Maiolino, R., Marconi, A., & Oliva, E. 2001a, A&A, 365, 37
Maiolino, R., Marconi, A., Salvati, M., et al. 2001b, A&A, 365, 28
Maiolino, R., & Rieke, G. H. 1995, ApJ, 454, 95
Maiolino, R., Shemmer, O., Imanishi, M., et al. 2007, A&A, 468, 979
Marconi, A., Risaliti, G., Gilli, R., et al. 2004, MNRAS, 351, 169
Marziani, P., Sulentic, J. W., Negrete, C. A., et al. 2015, Ap&SS, 356, 339
Marziani, P., Sulentic, J. W., Plauchu-Frayn, I., & del Olmo, A. 2013, A&A, 555, A89
Mazzucchelli, C., Bañados, E., Venemans, B. P., et al. 2017, ApJ, 849, 91
McLure, R. J., & Jarvis, M. J. 2002, MNRAS, 337, 109
Mejía-Restrepo, J. E., Lira, P., Netzer, H., Trakhtenbrot, B., & Capellupo, D. M. 2018a, NatAs, 2, 63
Mejía-Restrepo, J. E., Trakhtenbrot, B., Lira, P., & Netzer, H. 2018b, MNRAS, 478, 1929
Mejía-Restrepo, J. E., Trakhtenbrot, B., Lira, P., Netzer, H., & Capellupo, D. M. 2016, MNRAS, 460, 187
Merloni, A., Bongiorno, A., Bolzonella, M., et al. 2010, ApJ, 708, 137
Merloni, A., Bongiorno, A., Brusa, M., et al. 2014, MNRAS, 437, 3550
Netzer, H. 2019, MNRAS, 488, 5185
Oh, K., Koss, M., Markwardt, C. B., et al. 2018, ApJS, 235, 4
Oh, K., Yi, S. K., Schawinski, K., et al. 2015, ApJS, 219, 1
Oh, K., Koss, M. J., Ueda, Y., et al. 2022, ApJS, 261, 4
Oke, J. B., & Gunn, J. E. 1982, PASP, 94, 586
Onken, C. A., Ferrarese, L., Merritt, D., et al. 2004, ApJ, 615, 645
Onori, F., La Franca, F., Ricci, F., et al. 2017, MNRAS, 464, 1783
Osterbrock, D. E. 1981, ApJ, 249, 462
Paliya, V. S., Koss, M., Trakhtenbrot, B., et al. 2019, ApJ, 881, 154
Pancoast, A., Brewer, B. J., & Treu, T. 2014a, MNRAS, 445, 3055
Pancoast, A., Brewer, B. J., Treu, T., et al. 2014b, MNRAS, 445, 3073
Park, D., Woo, J.-H., Treu, T., et al. 2012, ApJ, 747, 30
Peterson, B. M. 2014, SSRv, 183, 253
Ramos Almeida, C., & Ricci, C. 2017, NatAs, 1, 679
Ricci, C., Trakhtenbrot, B., Koss, M. J., et al. 2017a, ApJS, 233, 17
Ricci, C., Trakhtenbrot, B., Koss, M. J., et al. 2017b, Natur, 549, 488
Ricci, F., La Franca, F., Marconi, A., et al. 2017c, MNRAS, 471, L41
Ricci, F., La Franca, F., Onori, F., & Bianchi, S. 2017d, A&A, 598, A51
Ricci, F., Triester, E., Bauer, F. E., et al. 2022, ApJS, 261, 8
Ricci, T. V., & Steiner, J. E. 2019, MNRAS, 486, 1138
Richards, G. T., Fan, X., Newberg, H. J., et al. 2002, AJ, 123, 2945
Richards, G. T., Kruczek, N. E., Gallagher, S. C., et al. 2011, AJ, 141, 167
Richards, G. T., Lacy, M., Storrie-Lombardi, L. J., et al. 2006, ApJS, 166, 470
Riffel, R., Rodríguez-Ardila, A., & Pastoriza, M. G. 2006, A&A, 457, 61
Rojas, A. F., Masetti, N., Minniti, D., et al. 2017, A&A, 602, A124
Rojas, A. F., Sani, E., Gavignaud, I., et al. 2020, MNRAS, 491, 5867
Runnoe, J. C., Brotherton, M. S., DiPompeo, M. A., & Shang, Z. 2014, MNRAS, 438, 3263
Runnoe, J. C., Brotherton, M. S., & Shang, Z. 2012, MNRAS, 422, 478
Schlegel, D. J., Finkbeiner, D. P., & Davis, M. 1998, ApJ, 500, 525
Schulze, A., Bongiorno, A., Gavignaud, I., et al. 2015, MNRAS, 447, 2085
Schulze, A., & Wisotzki, L. 2010, A&A, 516, A87
Shang, Z., Wills, B. J., Wills, D., & Brotherton, M. S. 2007, AJ, 134, 294
Shankar, F., Bernardi, M., Richardson, K., et al. 2019, MNRAS, 485, 1278
Shankar, F., Bernardi, M., Sheth, R. K., et al. 2016, MNRAS, 460, 3119
Shen, Y. 2013, BASI, 41, 61
Shen, Y., Greene, J. E., Strauss, M. A., Richards, G. T., & Schneider, D. P. 2008, ApJ, 680, 169
Shen, Y., & Ho, L. C. 2014, Natur, 513, 210
Shen, Y., & Liu, X. 2012, ApJ, 753, 125
Shen, Y., Wu, J., Jiang, L., et al. 2019, ApJ, 873, 35
Shimizu, T. T., Davies, R. I., Koss, M., et al. 2018, ApJ, 856, 154
Silk, J., & Rees, M. J. 1998, A&A, 331, L1
Smette, A., Sana, H., Noll, S., et al. 2015, A&A, 576, A77
Stern, D. 2015, ApJ, 807, 129
Stern, J., & Laor, A. 2012, MNRAS, 426, 2703
Storchi-Bergmann, T., Schimoia, J. S., Peterson, B. M., et al. 2017, ApJ, 835, 236
Suh, H., Civano, F., Trakhtenbrot, B., et al. 2020, ApJ, 889, 32
Trakhtenbrot, B., & Netzer, H. 2012, MNRAS, 427, 3081
Trippe, M. L., Crenshaw, D. M., Deo, R. P., et al. 2010, ApJ, 725, 1749
Vasudevan, R. V., Mushotzky, R. F., Winter, L. M., & Fabian, A. C. 2009, MNRAS, 399, 1553
Veilleux, S., Goodrich, R. W., & Hill, G. J. 1997a, ApJ, 477, 631
Veilleux, S., Sanders, D. B., & Kim, D.-C. 1997b, ApJ, 484, 92
Veilleux, S., Sanders, D. B., & Kim, D. C. 1999, ApJ, 522, 139
Veilleux, S., & Zheng, W. 1991, ApJ, 377, 89
Vernet, J., Dekker, H., D'Odorico, S., et al. 2011, A&A, 536, A105
Vestergaard, M., & Osmer, P. S. 2009, ApJ, 699, 800
Vestergaard, M., & Peterson, B. M. 2006, ApJ, 641, 689
Vietri, G., Mainieri, V., Kakkad, D., et al. 2020, A&A, 644, A175
Wang, J.-G., Dong, X.-B., Wang, T.-G., et al. 2009, ApJ, 707, 1334
Wenger, M., Ochsenbein, F., Egret, D., et al. 2000, A&AS, 143, 9
Winkler, H. 1992, MNRAS, 257, 677
Woo, J.-H., Schulze, A., Park, D., et al. 2013, ApJ, 772, 49
Woo, J.-H., Yoon, Y., Park, S., Park, D., & Kim, S. C. 2015, ApJ, 801, 38
Zheng, W., Veilleux, S., & Grandi, S. A. 1991, ApJ, 381, 418
Ziegler, B. L., & Bender, R. 1997, MNRAS, 291, 527